1 Response to comments of Dries Allaerts

- This paper aims to identify the optimal distribution of wind turbine set-points to mitigate flow blockage induced by atmospheric gravity waves and hence maximize wind-farm energy extraction. The authors simulate the response of the atmospheric flow to the wind-farm drag using a recently developed mid-fidelity model, and they introduce a corresponding optimization framework based on the continuous adjoint method. The results are promising and show that a non-uniform spatial distribution of wind turbine set points can increase the energy extraction of the farm by reducing the excitation of atmospheric gravity waves. I believe this paper is of interest to the wind energy community as it demonstrates the use of set-point optimization for wind farms and highlights the potential for new optimization and control strategies to cope with windfarm scale blockage.
  We would like to thank the referee for the kind words and the very constructive feedback in improving the quality of the paper.

- 1. Line 91: In the derivation of the three-layer model, no assumptions need to be made about the vertical component of the velocity. Rather, by averaging over the height of the respective layers, the horizontal momentum equations become independent of the vertical velocity.
  We have corrected our statement with the following sentences at P3-L90:

  "*The model equations are derived starting from the incompressible three-dimensional Reynolds-Averaged Navier-Stokes (RANS) equations for the ABL (Stull 1988). A depth-integration over the wind-farm and upper layer height is further computed, which removes the vertical velocity from the equations. Hence, the basic equation system is reduced to a set of only three equations: the continuity equation and the momentum equations in horizontal directions. Subsequently, the governing equations are linearized with respect to the background state variables, using some additional modelling assumptions for the turbulent stresses (see Allaerts and Meyers (2019) for more details).*"

- 2. Line 130: The relation between pressure and inversion layer displacement based on the complex stratification coefficient is not due to Gill 1982 (at least not the part concerning the atmospheric gravity waves). I think it is more appropriate to cite Smith 2010 instead.
  We agree on this. Hence, we have cited Smith 2010 instead of Gill 1982.

- 3. Eq. 17: Can you elaborate on the function of the complex stratification coefficient in the adjoint equations? That is, what do you mean with the negation of the arguments x and t. I assume this arrives from the partial integration and is similar to the sign reversal of the convective term, but it is not clear to me how I should interpret the current notation.
  The negation of the arguments x and t does not follow from partial integration. Rather, it follows from the following property. Given three functions $f, g, h \in L^1(\Omega)$, it can be shown

that

$$\begin{aligned}\int_\Omega \big[f(x) * g(x)\big] h(x) dx &= \int_\Omega \int_{\Omega'} \big[f(x-x')g(x')dx'\big] h(x) dx \\ &= \int_\Omega \int_{\Omega'} f(x-x')g(x')h(x)dx'dx \\ &= \int_{\Omega'} \int_\Omega f(x-x')h(x)dx g(x')dx' \\ &= \int_{\Omega'} \int_\Omega f(-(x'-x))h(x)dx g(x')dx' \\ &= \int_\Omega \big[f(-x) * h(x)\big] g(x) dx.\end{aligned}$$

Note that in the second passage we have changed the order of integration (Fubini's theorem). In the current application, this property allows us to write

$$-H_1 \int_0^T \iint_\Omega \Big[\mathcal{F}^{-1}(\hat{\Phi}) * \delta \boldsymbol{u}_1\Big] \cdot \nabla \Pi_1 d\boldsymbol{x} dt = -H_1 \int_0^T \iint_\Omega \Big[\mathcal{F}^{-1}(\hat{\Phi})(-\boldsymbol{x}, -t) * \nabla \Pi_1\Big] \cdot \delta \boldsymbol{u}_1 d\boldsymbol{x} dt.$$

To include this in the text, we have added the following sentence at P8-L213:

"*Note that the minus sign in the argument of $\mathcal{F}^{-1}(\hat{\Phi})(-\boldsymbol{x}, -t)$ is not a result from classical integration by parts, but arrives from applying Fubini's theorem to the convolution term in Eq. 12 and Eq. 13 (see Appendix A3 for details).*"

Moreover, we have also added the following lines at P24-L581:

"*Note that the minus sign in the argument of $\mathcal{F}^{-1}(\hat{\Phi})(-\boldsymbol{x}, -t)$ does not come from classical integration by parts. In fact, given three functions $f, g, h \in L^1(\Omega)$, it can be shown that*

$$\begin{aligned}\int_\Omega \big[f(x) * g(x)\big] h(x) dx &= \int_\Omega \int_{\Omega'} \big[f(x-x')g(x')dx'\big] h(x) dx \\ &= \int_{\Omega'} \int_\Omega f(-(x'-x))h(x)dx g(x')dx' \\ &= \int_\Omega \big[f(-x) * h(x)\big] g(x) dx.\end{aligned}$$

where in the second passage we have changed the order of integration (Fubini's theorem). This property allows us to write

$$-H_1 \int_0^T \iint_\Omega \Big[\mathcal{F}^{-1}(\hat{\Phi}) * \delta \boldsymbol{u}_1\Big] \cdot \nabla \Pi_1 \; d\boldsymbol{x} dt = -H_1 \int_0^T \iint_\Omega \Big[\mathcal{F}^{-1}(\hat{\Phi})(-\boldsymbol{x}, -t) * \nabla \Pi_1\Big] \cdot \delta \boldsymbol{u}_1 \; d\boldsymbol{x} dt.$$

"

- 4. Line 235: Can you comment on the numerical resources (time and number of processors if parallelized) it takes to compute an optimal set-point distribution? I am asking because a possible application could be using weather forecasts to update the set-point distribution when gravity waves are to be expected (e.g., forecast predicts shallow boundary layers in the next few hours).
  To include these information in the text, we have added the following paragraph at the end of section 3.1 (P10-L257):

  "*The solver (which is not parallelized) takes a couple of hours to solve the equations for*

a grid with resolution of 250 m (6.4×10^6 DOF per layer). Since convergence is reached after approximately 20 function evaluations (which means that we solve state and adjoint equations 20 times), the optimizer takes a couple of days to compute an optimal thrust set-point distribution. However, after this work was performed, we have upgraded the forward solver which is now 700 times faster than our previous version. Optimization of the backward solver is planned for the future, and we expect that this will lead to an optimization algorithm that will only take several minutes for the same case."

- 5. Line 241: How did you select the relative turbine spacing?
  In the study of Allaerts and Meyers (2019), the authors considered a rectangular shaped farm with length $L_x = 20$ km and width $L_y = 30$ km containing $N_t = 486$ turbines. These numbers where chosen to represent roughly the number of turbines and the area covered by the Belgian-Dutch wind-farm cluster. In our study, we select a wind-farm with the same dimensions. Moreover, to have a similar density of turbines in the farm, we fix the dimensionless turbine spacings to $s_x = s_y = 5.61$ so that $L_x L_y / s_x s_y D^2 \simeq 486$. To include this information, we have added the following sentence at P10-L267:

  "*The wind turbine relative spacings along the x- and y-direction are $s_x = s_y = 5.61$ (both non-dimensionalized with respect to the turbine rotor diameter D), so that the density of turbines in the farm is similar to the one of Allaerts and Meyers (2019) (i.e. leading to $\beta = 0.01$ in Eq. 8, setting both the wake efficiency η_w and γ to 0.9 as in Allaerts and Meyers (2018)). Note that we do not define a specific layout or a number of turbines but we only fix the density of turbines in the farm.*"

- 6. Line 301: Favourable pressure gradients are also present in the bulk of the wind farm, whereas the velocity deficits continue to increase throughout the farm and only recover behind the farm. I believe the favourable pressure gradients do not necessarily accelerate the flow, but are instead balanced by a higher thrust force. Physically, this would correspond to the favourable pressure gradient re-energizing the wake flows and thereby reducing the turbine losses in the bulk of the farm. Can you comment on this?
  We agree with the referee and we confirm that the sentence "*In both sub- and supercritical case, favourable pressure gradients develop within the wind-farm area which tend to accelerate the flow in the wind-farm exit region*" is misleading. In fact, favourable pressure gradients re-energize the waked flow reducing the velocity deficits in the bulk of the farm. This also partially explains the higher velocity deficits observed for the supercritical case over the wind-farm area if compared with the ones obtained in the subcritical case (the favourable pressure gradient is stronger in subcritical conditions than supercritical ones). Therefore, we have modified the sentence mentioned above to (P14-L341):

  "*In both sub- and supercritical case, favourable pressure gradients reduce the velocity deficits in the bulk of the farm.*"

- 7. Section 4.1: Did you consider optimizing for a uniform set-point distribution? What are the maximum gains to be expected there, and hence how much more is there to be gained by using a non-uniform set-point distribution? How would that uniform value compare to the average of the non-uniform distribution, and would the uniform value depend on the atmospheric condition as well?
  We thank the referee for the very insightful questions. To answer these questions, we have added the following section in the appendix (P28-L652):

  "*In the current section, we use the optimization framework derived in Section 2.2 to find an*

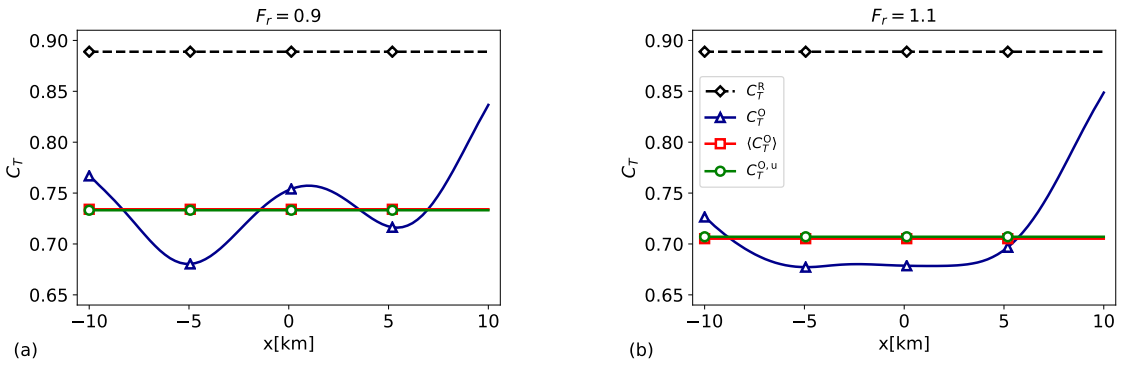

Figure 1: Reference thrust set-point (C_T^{R}), optimal non-uniform thrust set-point (C_T^{O}) and its averaged value over the wind-farm area $(\langle C_T^{\mathrm{O}} \rangle)$ and optimal uniform thrust coefficient distribution $(C_T^{\mathrm{O,u}})$ in (a) subcritical and (b) supercritical flow conditions. The C_T^{O} profiles are taken through the center of the farm ($y = 0$).

optimal uniform and steady thrust-coefficient distribution that minimizes the gravity-wave induced blockage effects. To avoid confusion, we will denote with C_T^{O} and $C_T^{\mathrm{O,u}}$ the optimal non-uniform and uniform distribution, respectively. The wind-farm layout and the atmospheric state are the ones detailed in Section 3.
Figure 1(a,b) displays the optimal spatially invariant $C_T^{\mathrm{O,u}}$ together with the streamwise profile of C_T^{O} through the center of the farm, and its averaged value over the wind-farm area $\langle C_T^{\mathrm{O}} \rangle$ for the sub- and supercritical case, respectively. Moreover, C_T^{R} denotes the thrust distribution used in the reference model. Interestingly, $C_T^{\mathrm{O,u}}$ corresponds to the average of the non-uniform distribution in both cases. Since C_T^{O} is sensitive to the atmospheric conditions, we expect $C_T^{\mathrm{O,u}}$ to depend as well on the atmospheric state (in fact, we observe a different value of $C_T^{\mathrm{O,u}}$ in sub- and supercritical conditions).
In the current example, the energy gain $\mathcal{G}$ (see Eq. 21 on article) over the reference model configuration obtained with the non-uniform distributions C_T^{O} are 5.3% and 7% for the sub- and supercritical case, respectively. For the optimal uniform distributions, we obtain an energy gain of 5% and 6.6%."

- 8. Section 4.1: How does the power performance of the optimal set-point distribution compare to the idealized power output when all turbines would be operating in isolated conditions? I.e. how much of the power loss due to flow blockage is irreversible?
  The usage of a box-function model makes it difficult to answer this question. In fact, this model uniformly spreads the force over the simulation cells in the wind-farm area and does not represent the disturbances caused by each turbine in detail. Therefore, the concept of turbines operating in isolated conditions is not reproducible. What we can do is to consider "turbines" which operate in idealized conditions, by using a uniform thrust set-point distribution with $C_T = 0.88$. This is what we have defined as reference case and the energy gains are referred to this state. The comparison suggested by the referee would be realizable if analytical wake models would be used (such as, the Gaussian wake model proposed by Niayifar and Porté-Agel (2014)). In order to not overload the discussion in the manuscript, we decided to not further explicitly comment on this. However, the wind-farm force model used in the optimization solver will be improved in the future, as suggested in the conclusions, and this will allow us to answer this question in more detail.

- * Line 389: Typo in "dispersive"
  * Label A12 and A13 reference the same equation split over two lines.
  * Line 573: Typo in "through"

Thank you, we have corrected these errata.

2 Response to comments of Anonymous Referee #2

- Interesting paper and concept. Contains every detail of the simulation but requires a solid background in fluid dynamics to understand.
  We would like to thank the referee for the constructive feedback in improving the quality of the paper.

- 1) The authors state on pg. 11 line 280: "However, all optimal.. ..are constant in time.. And conclude that unsteady time-periodic excitation is less effective" I believe that this claim is too strong. There is no guarantee that the optimizer will find the optimal solution. The optimizer finds a solution under the specified constraints, and that is what the authors present. This only has value if this gives rise to a better understanding of the physics. Now it is one of many possible solutions (local minima). The authors should consider rephrasing these claims to the assumptions made throughout the derivation.
  We fully agree with the referee's statement. Therefore, the following paragraph has been modified at P12-L307:

  "*The optimization model described in Section 2.2 is time and space dependent. Hence, the model is capable of finding a time-periodic optimal thrust-coefficient distribution over the wind-farm area in a fixed time interval* $[0, T]$*. However, all optimal thrust set-point distributions found for the different combinations of time horizons and time steps reported in Table 1, are constant in time. We have verified this using a range of steady and unsteady starting conditions for* C_T *in the algorithm, but did not find any unsteady optimum. We believe that this is due to two reasons. Firstly, we use steady-state inflow conditions, therefore neglecting meso-scale temporal variations in the velocity field (these could lead to time-dependent optimal control signals, but are not included in the current work). Secondly, the objective function is non-convex and there is no proof about the uniqueness of global minima. Hence, there is no guarantee that the optimal solution found by the optimizer corresponds to a global optimum. Nevertheless, since we do not observe any unsteady behaviour in our optimal solutions, we show only steady-state results in the remainder of the manuscript, and conclude for the time being that unsteady time-periodic excitation is less effective than a stationary spatially optimal distribution in this context.*
  We also note that our findings are in contrast with recent works of Goit and Meyers (2015), Munters and Meyers (2018) and Frederik et al. (2020), in which the authors illustrated the benefits of dynamic induction control over yaw and static induction control. However, the characteristic time scale of gravity-wave effects is estimated to be approximately 1 h (Gill 1982, Allaerts and Meyers 2019) which is an order of magnitude above the typical time scale of wake convection between turbines, and turbulent mixing in turbine wakes (this also justifies the larger sampling time used). Hence, while unsteadiness of the thrust coefficient (with a typical time scale of 50 seconds for large scale turbines) can lead to improved wake mixing (Goit and Meyers (2015), Munters and Meyers (2018), Frederik et al (2020)), it has no impact on phenomena that occur at larger time scales, such as wind-farm induced gravity waves."

- 2) The significance of the paper is also a bit unclear. In the conclusion the authors state that an optimization model was applied for set-point optimization. Many approximations have been made in the modelling step and there is no quantification of the potential error. The energy gains mentioned in the abstract are incredible high. I would like to see a validation of the model or the results applied to a high(er) validity model.
  We agree with the referee that we did not talk about the model validation. The constraints of our optimization model (the state equations) correspond to the same model derived by

Allaerts and Meyers (2019). This model has been validated in Allaerts and Meyers (2019) (see Section 3, VAL2) against LES results. The validation showed that the three-layer model outperforms the Smith (2010) model and agrees well with LES results for low perturbation values. To include this in the article, the following paragraph has been added at the end of section 2.1 (P6-L155):

"*The three-layer model configuration described above has been validated against LES results by Allaerts and Meyers (2019) (see Section 3 VAL2) on a two dimensional (x-z) domain (i.e., all spanwise derivatives are set to zero). The model shows a mean absolute error (MAE) of 1.3% and 1.8% in terms of maximum displacement of the inversion layer and maximum pressure disturbance, respectively. Moreover, the model underestimates the velocity over the wind-farm area with a MAE of 5.6%. Note that the three-layer model is a linearized model, hence the discrepancies with LES results increase with increasing perturbation values. In fact, the model agrees very well with LES data when perturbations are small (i.e, when non-linear effects are negligible). For further details, we refer to Allaerts and Meyers (2019).*"

Before to apply the results obtained to a higher validity model (i.e, our in-house LES solver SP-Wind), we need to improve the LES setup, which is what we will do in the near future. However, we did not mention it in the article, therefore we have added the following sentence to the last paragraph of the conclusions (P22-L531):

"*In the future, we also plan to apply the results obtained in this article to a higher fidelity model (i.e, our in-house LES solver SP-Wind). However, this requires some work on the efficiency of non-reflecting boundary conditions in our LES solver (Allaerts and Meyers 2017, 2018).*"

Finally, to avoid mentioning only the highest energy gain found in the abstract , we have modified the last sentence to (P1-L16):

"*Overall, energy gains above 4% were observed for 77% of the cases with peaks up to 14% for weakly stratified atmospheres in critical flow regimes.*"

- 3) Generally, assumptions should be stated clearly. For example, the wakes between the turbines are not explicitly modelled. This is a large assumption to make, and is only briefly mentioned in the text. What is the expected impact on the results? How does it affect the conclusions drawn in the article? Also, the sampling time seems rather large for typical wind farm control algorithms. How does this impact your results? Would you be able to find a periodic optimal signal if you had a shorter sampling time? How about the fidelity of your rotor model – would things change with an ALM model?
  We agree with the referee that the sentence "the wakes between the turbines are not explicitly modelled" is misleading. To model the farm drag force, we use a box-function wind-farm force model (also used in Smith (2010) and Allaerts and Meyers (2019)) which uniformly spreads the force over the simulation cells in the wind-farm area and does not represent the disturbances caused by each turbine in detail. The force magnitude depends on the wind-farm layout (see parameter β), the wind speed, and the thrust-coefficient distribution (i.e., the C_T value in every grid cell within the farm). To avoid confusion, we have modified the sentence to (P4-L111):

  "*We use a box-function wind-farm force model similar to Smith (2010) in our study. This al-*

lows us to avoid the complexity of wake models while gaining in computational time. In fact, this model uniformly spreads the force over the simulation cells in the wind-farm area and does not represent the disturbances caused by each turbine in detail. The force magnitude depends on the wind-farm layout, the wind speed and the thrust set-point distribution (i.e., the C_T value in every grid cell within the farm)."

To understand how this simple wind-farm model affects the conclusion drawn in the article, it is useful to compare the three-layer model predictions using both the model previously discussed and the Gaussian wake model, which are shown in Allaerts and Meyers (2019) (VAL2 and VAL3, respectively). Although the magnitude of the predictions are slightly different, the trends are unchanged. Hence, we expect that trends may remain the same if a more accurate force model would be used. Nevertheless, the accuracy of the results could benefit from an improved force model (this also answer to the question regarding the ALM). Future work needs to focus on further improving the model, as well as on validation.

Regarding the question on the sampling time, gravity waves have a different time scale than wake convection, which justifies the larger sampling time used. We have added this consideration in Section 4.1 (see second comment). We have also tried to use smaller sampling time (i.e, down to a couple of seconds) but the optimizer has never found an unsteady optimum.

- 4) The article is long, making it cumbersome to read. Perhaps certain parts can be omitted. For example, is the model from section 2.1 a novel contribution or is it identical to the one described in Allaerts and Meyers 2019? If the latter, consider removing it from this article.
  The model described in section 2.1 is similar to the one discussed in Allaerts and Meyers (2019), but nevertheless, we have added the time dependency to the equations, a different equations' form is used, and the wind-farm force model is different. Therefore, we believe that a brief explanation of the model equations makes the article more understandable (the model description occupies approximately a page and a half, excluding the wind-farm force model). This is the reason why we decided to include this section in the article. However, to reduce the length of the section (and of the article in general), we have deleted some unnecessary sentences and explanations from the text.

- 5) Figure 1: It seems as if you have very few iterations before convergence. Can you comment on this?
  Figure 1 shows that the cost function decreases rapidly in the firsts two to three iterations, reaching convergence after approximately 5 algorithm iterations. The use of a quasi-Newton method in combination with the limited complexity of our optimization model (for instance, the constraints are linearized equations) allow us to reach such a fast convergence (e.g., note that a Newton method reaches convergence in one step for a classical convex QP, i.e. convex quadratic cost function with linear constraints). Moreover, the continuous adjoint method limits the number of function evaluations, since it is not necessary to evaluate $\tilde{\mathcal{J}}(C_T + \alpha\delta C_T)$ for all directions δC_T in the control space (at the expenses of solving an auxiliary set of equations). Based on this, we were not surprised in reaching convergence after 6 L-BFGS iterations with only 20 function evaluations. To include these considerations in the article, we have added the following sentence in section 3.1 (P9-L246):

  "*Fig. 1 shows that the cost function decreases rapidly in the firsts two to three algorithm iterations, reaching a plateau afterwards. The use of a quasi-Newton method in combination with the limited complexity of our optimization model (for instance, the constraints are*

linearized equations) allow us to reach such a fast convergence. Moreover, the continuous adjoint method limits the number of function evaluations, since it is not necessary to evaluate $\tilde{\mathcal{J}}(C_T + \alpha\delta C_T)$ for all directions δC_T in the control space (at the expenses of solving an auxiliary set of equations)."

3 Response to comments of Alan Wai Hou Lio

- The paper is interesting. The authors investigated the problems of the mesoscale interaction between a wind farm and atmospheric boundary-layer. A three-layer model is proposed for modelling the wind-farm induced gravity wave. Based on the simplified model, optimisation is then proposed to find the optimal thrust coefficient distributions that maximise the wind farm power output. The concept is appealing and the topic is definitely relevant to the wind energy community.
  We would like to thank the referee for the constructive feedback in improving the quality of the paper.

- Comments: pg1: Some claims by the authors were not clear. For example, the optimal thrust coefficient distributions are spatially stationary rather than time-periodic. Did the authors consider turbulent wind inflow and turbine-to-turbine interactions? Does the claim imply that stationary spatial distributions of thrust coefficients are better than dynamically changing the thrust set-points for maximising the wind farm power? This claim disagreed with some of the other works (e.g. [1]). In [1], the benefit of periodic dynamic induction control was shown, where the thrust coefficient of the upstream turbine was periodically adjusted to improve the downstream wind flow. How is this work related to [1]?
  The referee is right in saying that our claims disagree with some previous works. Although our study deals with much larger scales than the ones usually considered in dynamic or static induction control, we believe that it is useful to relate it with other recent findings. Hence, the following paragraph has been modified at P12-L307:

  "*The optimization model described in Section 2.2 is time and space dependent. Hence, the model is capable of finding a time-periodic optimal thrust-coefficient distribution over the wind-farm area in a fixed time interval* $[0, T]$*. However, all optimal thrust set-point distributions found for the different combinations of time horizons and time steps reported in Table 1, are constant in time. We have verified this using a range of steady and unsteady starting conditions for* C_T *in the algorithm, but did not find any unsteady optimum. We believe that this is due to two reasons. Firstly, we use steady-state inflow conditions, therefore neglecting meso-scale temporal variations in the velocity field (these could lead to time-dependent optimal control signals, but are not included in the current work). Secondly, the objective function is non-convex and there is no proof about the uniqueness of global minima. Hence, there is no guarantee that the optimal solution found by the optimizer corresponds to a global optimum. Nevertheless, since we do not observe any unsteady behaviour in our optimal solutions, we show only steady-state results in the remainder of the manuscript, and conclude for the time being that unsteady time-periodic excitation is less effective than a stationary spatially optimal distribution in this context.*
  We also note that our findings are in contrast with recent works of Goit and Meyers (2015), Munters and Meyers (2018) and Frederik et al. (2020), in which the authors illustrated the benefits of dynamic induction control over yaw and static induction control. However, the characteristic time scale of gravity-wave effects is estimated to be approximately 1 h (Gill 1982, Allaerts and Meyers 2019) which is an order of magnitude above the typical time scale of wake convection between turbines, and turbulent mixing in turbine wakes (this also justifies the larger sampling time used). Hence, while unsteadiness of the thrust coefficient (with a typical time scale of 50 seconds for large scale turbines) can lead to improved wake mixing (Goit and Meyers (2015), Munters and Meyers (2018), Frederik et al (2020)), it has no impact on phenomena that occur at larger time scales, such as wind-farm induced gravity waves."

- pg2 l59: “asses” -> asks.
  Thank you, we have corrected this erratum.

- pg4 l116: Ct is a function of Ct(x,y,t)? What is x and y in B(x,y)?
  To avoid the influence of the wind-farm layout on the results presented, the wind profile is always oriented along the x-axis. Hence, the x- and y-axis denote the streamwise and spanwise direction, respectively. The function $B(x, y)$ is a box function equal to one for the (x, y) coordinates within the wind-farm area and zero elsewhere. Similarly, the thrust-coefficient distribution $C_{\mathrm{T}}(x, y, t)$ is function of the spatial coordinate x and y and of the time t. The thrust- and power-coefficient distribution are always multiplied by the box function $B(x, y)$ in the text, since they are defined only within the wind-farm area.The following sentence has been added at P5-L122:

  “*the x- and y-axis denote the streamwise and spanwise direction, respectively.*”

- pg5 l123: What is the dimension of Ct? Is Ct a vector where the number of elements in that vector is equal to the number of turbines? How is Ct of each turbine related the aggregate wind farm drag f?
  $C_T = C_T(x, y, t)$ denotes the thrust set-point distribution and can be represented mathematically as $C_T : \mathbb{R}^2 \times [0, T] \rightarrow \mathbb{R}$. In the text, the thrust-coefficient distribution is always multiplied by the box function $B(x, y)$ (see previous comment) so that it assumes non-zero values only within the wind-farm area. If we denote with N_x^{wf} and N_y^{wf} the number of grid points within the farm along the x- and y-direction, $N_x^{\mathrm{wf}} N_y^{\mathrm{wf}}$ represents the number of grid cells in the farm area. We assume a constant C_T value in every cell, and each of these values represent a control parameter of our optimization problem. Hence, the number of control parameters is given by $N_x^{\mathrm{wf}} N_y^{\mathrm{wf}} N_t$ (this is mentioned in the article at P7-L190).

  In regards to the last question, note that we select the turbine spacings s_x and s_y to have a density of turbines in the farm similar to the one of Allaerts and Meyers (2019) (i.e. leading to $\beta = 0.01$ in Eq. 8, using $\eta_w = 0.9$ and $\gamma = 0.9$ similar to Allaerts and Meyers (2018)). Hence, we fix the density of turbine in the farm but we do not specifically define a layout or a number of turbines. In fact, the force model uniformly spreads the force over the simulation cells in the wind-farm area and the number of grid cells within the farm define the DOF of our optimization problem (as mentioned above). The turbine spacings (together with other parameters) only define the wind-farm drag-force magnitude. In order to compute the thrust-coefficient $\tilde{C}_{T,k}(t)$ of a turbine at location (x_k, y_k), it is possible to evaluate the thrust coefficient distribution $C_T(x_k, y_k, t)$. A more accurate connection between $\tilde{C}_{T,k}(t)$ and the drag force $\boldsymbol{f}$ would require the use of an analytical wind-farm model, but this is out of the scope of the current work. To include these information in the text, we have added the following sentence at P5-L127:

  “*Finally, $C_T(x, y, t)$ represents the thrust-coefficient distribution. To compute the thrust coefficient $\tilde{C}_{T,k}(t)$ of a turbine at location (x_k, y_k), it is possible to evaluate the thrust set-point distribution $C_T(x_k, y_k, t)$. A more accurate connection between $\tilde{C}_{T,k}(t)$ and the drag force $\boldsymbol{f}$ would require the use of an analytical wind-farm model, but this is out of the scope of the current work.*”

  Moreover, we have also mentioned at P10-L267 that:

  “*The wind turbine relative spacings along the x- and y-direction are $s_x = s_y = 5.61$ (both non-dimensionalized with respect to the turbine rotor diameter D), so that the density of*

turbines in the farm is similar to the one of Allaerts and Meyers (2019) (i.e. leading to $\beta = 0.01$ in Eq. 8, setting both the wake efficiency η_w and γ to 0.9 as in Allaerts and Meyers (2018)). Note that we do not define a specific layout or a number of turbines but we only fix the density of turbines in the farm."

- p5 l124: "the thrust-coefficient distribution Ct has to be interpreted as a perturbation." Is Ct the thrust coefficient or the perturbation to the thrust coefficient?
  The equations are linearized with respect to the background state variables, that is around a state for which the wind-farm is not operating. Hence, there is no distinction between the thrust coefficient C_{T} and its perturbation C'_{T} . In fact, $C_{\mathrm{T}} = C^{\mathrm{b}}_{\mathrm{T}} + C'_{\mathrm{T}}$ but we are linearizing around a non-operating wind farm, therefore $C^{\mathrm{b}}_{\mathrm{T}} = 0$ and $C_{\mathrm{T}} = C'_{\mathrm{T}}$. However, in an attempt to reduce the length of the article (suggested by the Anonymous Referee #2), we have decided to remove this sentence from the text (a similar explanation is already written in Allaerts and Meyers (2019)).

- "The goal of the optimization framework is to find a time-periodic optimal thrust-coefficient distribution". Why did the authors assume that the optimal thrust distribution would be time-periodic in the beginning?
  We are using steady environmental conditions. Hence, if we use a control signal for a finite time window $[0, T]$, since nothing changes in the atmospheric conditions, the only option is that the signal repeats itself (at least if we want to arrive at a control that is on average steady) in the time window $[T, 2T]$, and so on. To include this information in the article, we have modified the text as follows (P6-L163):

  "*The goal of the optimization framework is to find a time-periodic optimal thrust-coefficient distribution $C^{\mathrm{O}}_T(x, y, t)$ that minimizes the gravity-wave induced blockage effects, maximizing the flow wind speed and consequently the wind-farm energy extraction over a selected time period T. The background atmospheric state is presumed to be steady, which is the reason why we use a time-periodic control (i.e. leading to a moving time average of the optimal control that is steady, and does not lead to end-of-time effects).*"

- p6: Equation (13), what is $\boldsymbol{\psi}$ and J in (13) is not a function of Ct. I suggest the authors swap equation (13) and (14) for clarity.
  $\boldsymbol{\psi}$ is the vector containing the state variables and is defined in P7-L189.
  Correction (P6-L169):

  "*We have swapped equation (13) with equation (14) as suggested by the referee. Hopefully this will help in clarifying the dependence of J on C_{T}.*"

- p7 l183: $\mathcal{N}(\boldsymbol{\psi}(C_t), C_t) = 0$. Is this only valid around the neighbourhood of the solution? What is $\mathcal{N}$?
  The vector $\boldsymbol{\psi}$ contains the state variables, hence it depends upon the thrust coefficient distribution. We denote with $\boldsymbol{\psi}(C_T)$ the solution of the state equation. $\mathcal{N}\big(\boldsymbol{\psi}, C_T\big)$ is an operator which represents the state equations. If $\boldsymbol{\psi}(C_T)$ is a solution, then $\mathcal{N}\big(\boldsymbol{\psi}(C_T), C_T\big)$=0. This does not hold in the neighbourhood of the solution but only for $\boldsymbol{\psi}(C_T)$ which satisfies the state equations. The sentence has been changed to (P7-L195):

  "*To avoid exploring the entire feasibility region, we require $\boldsymbol{\psi}(C_T)$ to be the solution of the state equations throughout the optimization process. In other words, defining an operator $\mathcal{N}\big(\boldsymbol{\psi}, C_T\big)$ that denotes the state equations, we are enforcing $\mathcal{N}\big(\boldsymbol{\psi}(C_T), C_T\big) = 0$ during optimization iterations.*"

- p11 l268: what is P_N?
  The non-dimensional number P_N is defined as $P_N = U_B^2/NH\|\boldsymbol{U}_g\|$ where N is the Brunt-Väisälä frequency. This number is an indicator of the effects of internal waves in the troposphere. For instance, low P_N values correspond to strongly stratified atmosphere which in turn implies strong excitation of internal waves. The following sentence has been added (P12-L298):

  "*Further, P_N expresses the impact of internal waves in the troposphere which increases when P_N decreases. The background state defined in Table 1 leads to $P_N = 1.92$.*"

Set-point optimization in wind farms to mitigate effects of flow blockage induced by gravity waves

Luca Lanzilao and Johan Meyers

Department of Mechanical Engineering, KU Leuven, Celestijnenlaan 300 A, 3001 Leuven, Belgium

Correspondence: Luca Lanzilao (luca.lanzilao@kuleuven.be)

Abstract. Recently, it has been shown that flow blockage in large wind farms may lift up the top of the boundary layer, thereby triggering atmospheric gravity waves in the inversion layer and in the free atmosphere. These waves impose significant pressure gradients in the boundary layer causing detrimental consequences in terms of farm's efficiency. In the current study, we investigate the idea of controlling the wind farm in order to mitigate the efficiency drop due to wind-farm induced gravity waves and blockage. The analysis is performed using a fast boundary layer model which divides the vertical structure of the atmosphere into three layers. The wind-farm drag force is applied over the whole wind-farm area in the lowest layer and is directly proportional to the wind-farm thrust set-point distribution. We implement an optimization model in order to derive the thrust-coefficient distribution which maximizes the wind-farm energy extraction. We use a continuous adjoint method to efficiently compute gradients for the optimization algorithm, which is based on a quasi-Newton method. Energy gains are evaluated with respect to a reference thrust-coefficient distribution based on the Betz–Joukowsky set point. We consider thrust coefficients that can change in space, as well as in time, i.e. considering time-periodic signals. However, in all our optimization results, we find that optimal thrust-coefficient distributions are steady; any time-periodic distribution is less optimal. The (steady) optimal thrust-coefficient distribution is inversely related to the vertical displacement of the boundary layer. Hence, it assumes a sinusoidal behaviour in the streamwise direction in subcritical flow conditions, whereas it becomes a U-shaped curve when the flow is supercritical. The sensitivity of the energy gain to the atmospheric state is studied using the developed optimization tool for almost two thousand different atmospheric states. ~~Energy gains of~~ Overall, energy gains above 4% were observed for 77% of the cases with peaks up to 14% ~~are found~~ for weakly stratified atmospheres in critical flow regimes.

1 Introduction

Nowadays, it is well known that turbines strongly interact when clustered together in large arrays, increasing the momentum deficit in the lowest region of the atmospheric boundary-layer (ABL). These turbine–turbine interactions, such as reduced wind speed and increased turbulence intensity, occur within the wind-farm area and can lead to detrimental consequences in terms of farm's efficiency (Barthelmie et al., 2010). However, it has been recently discovered that also non-local effects such as gravity waves may have strong implications on the wind-farm energy extraction (Allaerts and Meyers, 2018, 2019).

Wind-farm induced gravity waves are triggered by the upward displacement of the boundary layer which is caused by diverging fluid streamlines due to flow deceleration. As a result, an adverse pressure gradient develops in the induction region of

the wind farm, which slows down the wind-farm inflow velocity, reducing the farm efficiency. The goal of the current study is to determine a wind-farm thrust-coefficient distribution that minimizes the gravity-wave induced blockage effects, maximizing the flow wind speed, and therefore the energy extraction. Moreover, we investigate the impact of different atmospheric conditions on the optimal thrust-coefficient distribution and corresponding energy gains.

The cumulated blockage effect induced by the wind farm in the induction region was associated with wind-farm induced gravity waves only in recent years. In the pioneering work of Smith (2010), a quasi-analytical model of atmospheric response to wind-farm drag was used for modelling gravity-wave excitation due to diverging streamlines above the wind-farm area. Results have shown that gravity-wave excitation is strongly dependent upon the height of the boundary layer and the stability of the atmosphere aloft. Later, a fast boundary-layer model was proposed by Allaerts and Meyers (2019) who highlighted the crucial role of the inversion layer in determining gravity-wave patterns. The authors also used this model for an annual energy production study of the Belgian-Dutch offshore wind-farm cluster, showing that the annual energy loss due to the effect of self-induced gravity waves might be on the order of 4 to 6% (Allaerts et al., 2018).

Gravity waves were also observed in mesoscale and Large Eddy Simulation (LES) models. Fitch et al. (2012) and Volker (2014) proposed two different wind-farm parametrizations for the Weather Research and Forecasting model (WRF). Wind-farm induced gravity waves were observed in both cases, causing flow deceleration several kilometers upstream of the farm. Allaerts and Meyers (2017, 2018) have investigated the interaction between an "infinitely" wide wind farm and both a conventionally neutral and stable boundary layer in typical offshore conditions in a LES framework. They found that for low ABL heights, gravity waves induce strong pressure gradients and play an important role in the distribution of the kinetic energy within the farm. Wu and Porté-Agel (2017) considered a large finite-size wind farm operating in a conventionally neutral boundary layer (CNBL) with different free atmosphere stratification, and they conclude that strongly stratified atmospheres decrease the turbine power output up to 35% with respect to the weakly stratified cases. Blockage effects were also detected in field measurements. Wind speed data taken before and after the placement of three wind farms showed that there was a reduction in wind speed of about 3% in the induction region of each wind farm after that turbines were installed (Bleeg et al., 2018).

In the past years, a considerable amount of research has focused on wind-farm control strategies that allow to maximize the farm power output. Wake redirection techniques and decreasing set points of first row turbines are different strategies example. Goit and Meyers (2015) considered the individual wind turbines as flow actuators; the thrust set points were dynamically changed to obtain an optimal flow field which minimized the turbine interactions. Energy gains up to 16% were obtained with respect to uncontrolled cases. Gebraad et al. (2016) and Quick et al. (2017) used static yaw techniques to redirect first row turbines wake to increase the available power for downwind turbines. Munters and Meyers (2018) combined the two strategies, showing "power gains that approximate the sum of those achieved by each control strategy separately". The wind-farm layout also plays a crucial role in power extraction. Meyers and Meneveau (2012) and Stevens (2016) used optimization tools to find the optimal turbine spacing in fully-developed and finite-sized wind farm, respectively. However, all optimization models mentioned above neglect wind-farm–ABL interactions that take place at mesoscale, such as wind-farm induced gravity waves. In this paper, we develop an optimization model which takes into account self-induced gravity-wave effects and we

asses investigate whether it is possible to mitigate the gravity-wave induced blockage effects by varying the thrust set-point distribution within the wind-farm area.

Despite the detailed flow information that LES models provide, their high computational cost makes their applicability to optimization and sensitivity studies challenging. Therefore, in the current paper we use a fast boundary-layer model proposed by Allaerts and Meyers (2019) which divides the vertical structure of the atmosphere into three layers (from here the name three-layer model) and we reformulate it as an optimization problem. The objective function is defined as the wind-farm energy extracted over a time period T, while the constraints are the model equations plus a box constraint for the wind-farm thrust set-point distribution $C_T(x, y, t)$. The model equations are derived following the theory for interacting gravity waves and boundary layers developed by Smith et al. (2006), Smith (2007) and Smith (2010). Consequently, the optimal thrust-coefficient distribution computed using the optimization formulation of the three-layer model takes into account the effects of self-induced gravity waves.

The remainder of this paper is formulated as follows. The three-layer model and its optimization formulation is introduced in Section 2. Next, Section 3 describes the numerical setup, wind-farm layout and atmospheric state. Thereafter, Section 4 presents optimization results. The optimal thrust set-point distributions obtained in two different flow cases are discussed in Section 4.1. The sensitivity of the energy gain to the atmospheric state is carried out in Section 4.2. Finally, conclusions and suggestions for further research are given in Section 5 .

2 Methodology

We now introduce the approach used for modelling wind-farm induced gravity waves and the method applied for maximizing the wind-farm energy output. The three-layer model is described in Section 2.1 and its optimization formulation is derived in Section 2.2.

2.1 Three-layer model

In the work of Smith (2010), the atmospheric response to wind-farm drag is simulated by dividing the vertical structure of the atmosphere in two layers: the ABL and the free atmosphere aloft. This approach has strong limitations. In fact, the author is implicitly assuming that the turbine drag is mixed homogeneously between turbine level and the top of the ABL. In real wind farms, the turbine drag slows down the flow only within few hundreds meters from the ground level, triggering the formation of an internal boundary layer (Wu and Porté-Agel, 2013; Allaerts and Meyers, 2017). To overcome the limitations of Smith's model, the three-layer model divides the ABL into two layers: the wind-farm layer in which the turbine forces are felt directly (a layer's height of twice the turbine hub height has been used by Allaerts and Meyers (2019) based on insights from LES in Allaerts et al. (2018)), and a second layer up to the top of the ABL. Finally, the third layer models the free atmosphere above the ABL following the approach of Smith (2010).

The model equations are derived starting from the incompressible three-dimensional Reynolds-Averaged Navier-Stokes (RANS) equations for the ABL (Stull, 1988). The vertical component of the velocity field is a lot smaller than the horizontal

components in the ABL. Moreover, it is reasonable to assume a hydrostatic pressure distribution. These assumptions allow to reduce A depth-integration over the wind-farm and upper layer height is further computed, which removes the vertical velocity from the equations. Hence, the basic equation system is reduced to a set of only three equations: the continuity equation and the momentum equations in horizontal directions. FinallySubsequently, the governing equations are averaged over the wind-farm and upper layer height, and further linearized with respect to the background state variables, using some additional modelling assumptions for the turbulent stresses (see Allaerts and Meyers (2019) for more details). As a result, we are using the following equations for the two layers in the ABL

$$\frac{\partial \boldsymbol{u}_1}{\partial t} + \boldsymbol{U}_1 \cdot \nabla \boldsymbol{u}_1 + \frac{1}{\rho_0}\nabla p + f_c \boldsymbol{J} \cdot \boldsymbol{u}_1 - \nu_{t,1}\nabla^2 \boldsymbol{u}_1 - \frac{\boldsymbol{D}'}{H_1} \cdot \big(\boldsymbol{u}_2 - \boldsymbol{u}_1\big) + \frac{\boldsymbol{C}'}{H_1} \cdot \boldsymbol{u}_1 = \frac{\boldsymbol{f}}{H_1}, \tag{1}$$

$$\frac{\partial \eta_1}{\partial t} + \boldsymbol{U}_1 \cdot \nabla \eta_1 + H_1 \nabla \cdot \boldsymbol{u}_1 = 0, \tag{2}$$

$$\frac{\partial \boldsymbol{u}_2}{\partial t} + \boldsymbol{U}_2 \cdot \nabla \boldsymbol{u}_2 + \frac{1}{\rho_0}\nabla p + f_c \boldsymbol{J} \cdot \boldsymbol{u}_2 - \nu_{t,2}\nabla^2 \boldsymbol{u}_2 + \frac{\boldsymbol{D}'}{H_2} \cdot \big(\boldsymbol{u}_2 - \boldsymbol{u}_1\big) = 0, \tag{3}$$

$$\frac{\partial \eta_2}{\partial t} + \boldsymbol{U}_2 \cdot \nabla \eta_2 + H_2 \nabla \cdot \boldsymbol{u}_2 = 0. \tag{4}$$

When the wind farm is not operating (i.e., the wind-farm drag force is zero), a horizontally invariant reference state $\big(\boldsymbol{U}_1, H_1\big)$ and $\big(\boldsymbol{U}_2, H_2\big)$ characterizes the wind-farm and upper layer, where $\boldsymbol{U}_1 = \big(U_1, V_1\big)$ and $\boldsymbol{U}_2 = \big(U_2, V_2\big)$ are the height-averaged horizontal components of the background velocity and H_1, H_2 represent the height of the two layers. Whenever the farm extracts power from the flow, small velocity and height perturbations $\big(\boldsymbol{u}_1, \eta_1\big)$ and $\big(\boldsymbol{u}_2, \eta_2\big)$ are triggered. The equations derived by Allaerts and Meyers (2019) predict the spatial evolution of these perturbations. In this article, we also consider the temporal evolution, and thus, the relevant time derivatives are added to the equations. Furthermore, ρ_0 denotes the air density, assumed constant within the ABL, $\nu_{t,1}$ and $\nu_{t,2}$ are the depth-averaged turbulent viscosity, $f_c = 2\Omega \sin\phi$ is the Coriolis frequency, with Ω the angular velocity of the earth and ϕ the latitude, $\boldsymbol{J} = \boldsymbol{e}_x \otimes \boldsymbol{e}_y - \boldsymbol{e}_y \otimes \boldsymbol{e}_x$ is the two-dimensional rotation dyadic with $\boldsymbol{e}_x$ and $\boldsymbol{e}_y$ two-dimensional unit vectors in the x- and y-direction, respectively. Finally, the perturbation of the friction at the ground and at the interface between both layers are described by the matrices $\boldsymbol{C}'$ and $\boldsymbol{D}'$.

The right-hand side of Eq. 1 is characterized by the wind-farm drag force $\boldsymbol{f}$. To limit the computational cost, we We use a box-function wind-farm force model similar to Smith (2010) . Therefore, we do not include the wake effects of each wind turbine individually, but instead we assume that the drag force is distributed over the whole in our study. This allows us to avoid the complexity of wake models while gaining in computational time. In fact, this model uniformly spreads the force over the simulation cells in the wind-farm area . and does not represent the disturbances caused by each turbine in detail. The force magnitude depends on the wind-farm layout, the wind speed and the thrust set-point distribution (i.e., the C_T value in every grid cell within the farm). As for the flow equations, the wind-farm drag force model is linearized around a constant background state. We retain the first two terms of the Taylor expansion; both scale linearly with the thrust-coefficient distribution. Hence,

the drag force is given by $\boldsymbol{f} = \boldsymbol{f}^{(0)} + \boldsymbol{f}^{(1)}$ with

$$\boldsymbol{f}^{(0)} = -\beta C_T B(x,y) \|\boldsymbol{U}_1\| \boldsymbol{U}_1, \tag{5}$$

$$\boldsymbol{f}^{(1)} = -\beta \frac{C_T B(x,y)}{\|\boldsymbol{U}_1\|} C_T B(x,y) \boldsymbol{U}_{11+1}{}^{2\prime} \cdot \boldsymbol{u}_1, \tag{6}$$

where

$$\boldsymbol{U}' = \frac{1}{\|\boldsymbol{U}_1\|} \left(\boldsymbol{U}_1 \otimes \boldsymbol{U}_1 + \boldsymbol{I} \|\boldsymbol{U}_1\|^2 \right) \tag{7}$$

and with $B(x,y)$ a box function equal to one within the wind-farm area and zero outside. The x- and y-axis denote the streamwise and spanwise direction, respectively. The wind-farm drag force magnitude in Eqs. 5 and 6 scales with

$$\beta = \frac{\pi \eta_w \gamma}{8 s_x s_y}, \tag{8}$$

where s_x and s_y are the streamwise and spanwise turbine spacing relative to the rotor diameter, η_w is the wake efficiency and $\gamma = u_r^2 / \|\boldsymbol{U}_1\|^2$ is a velocity shape factor with u_r the rotor-averaged wind speed (Allaerts and Meyers, 2018). Moreover, $\boldsymbol{I} = \boldsymbol{e}_x \otimes \boldsymbol{e}_x + \boldsymbol{e}_y \otimes \boldsymbol{e}_y$ denotes the unit dyadic. Finally, $C_T(x,y,t)$ ~~is~~ represents the thrust-coefficient distribution. ~~Since we linearize the equation around a background state for which the wind-farm is not operating,~~ To compute the thrust coefficient $\tilde{C}_{T,k}(t)$ of a turbine at location (x_k, y_k), it is possible to evaluate the thrust set-point distribution $C_T(x_k, y_k, t)$. A more accurate connection between $\tilde{C}_{T,k}(t)$ and the ~~thrust-coefficient distribution C_T has to be interpreted as a perturbation. Hence, $\boldsymbol{f}^{(0)}$ and $\boldsymbol{f}^{(1)}$ technically represent the first-order and second-order cross term of the Taylor expansion. Finally, $\boldsymbol{I} = \boldsymbol{e}_x \otimes \boldsymbol{e}_x + \boldsymbol{e}_y \otimes \boldsymbol{e}_y$ is the unit dyadic~~drag force $\boldsymbol{f}$ would require the use of an analytical wind-farm model, but this is out of the scope of the current work. Relation 6 is nonlinear since it contains a product between time and space-dependent variables (i.e, C_T and $\boldsymbol{u}_1$). We decide to retain this term because it allows us to include gravity-wave feedback on wind-farm energy extraction. In fact, $\boldsymbol{f}^{(1)} \geq 0$ so that it reduces the drag force that the farm exerts on the flow, thereby reducing effects of blockage in the model.

The total vertical displacement of the inversion layer $\eta_t = \eta_1 + \eta_2$ triggers gravity waves which induce pressure perturbations p. The relation between these two quantities is given by ~~(Gill, 1982)~~ Smith (2010)

$$\frac{p}{\rho_0} = \mathcal{F}^{-1} \Phi(\hat{\Phi}) * \eta_t \tag{9}$$

where $\mathcal{F}^{-1}$ and $*$ denote the inverse Fourier transform and the convolution product, respectively. The pressure p is evaluated at the capping inversion height and it is assumed to be constant through the whole ABL (using the classical boundary-layer approximation $\partial p / \partial z = 0$). The complex stratification coefficient ~~Φ~~ $\hat{\Phi}$ in Fourier components is expressed as

$$\Phi\hat{\Phi} = g' + \frac{i\left(N^2 - \Omega^2\right)}{m}. \tag{10}$$

Relation 10 is obtained from linear three-dimensional, non-rotating, non-hydrostatic gravity-wave theory (Nappo, 2002) under the assumption of constant wind speed $\boldsymbol{U}_g = \left(U_g, V_g\right)$ and Brunt-Väisälä frequency N. The reduced gravity $g' = g\Delta\theta/\theta_0$

accounts for two-dimensional trapped lee waves (further named as inversion waves) which corrugate the capping inversion layer. The potential-temperature difference $\Delta\theta$ denotes the strength of the capping inversion, and θ_0 is a reference potential temperature. The effect of internal gravity waves is represented by the second term of relation 10, where m denotes the vertical wavenumber which is given by

$$m^2 = \left(k^2 + l^2\right)\left(\frac{N^2}{\Omega^2} - 1\right). \tag{11}$$

According to the sign of m^2 we can have propagating or evanescent waves. Moreover, $\Omega = \omega - \kappa \cdot \boldsymbol{U}_g$ denotes the intrinsic wave frequency with $\kappa = (k, l)$ the horizontal wavenumber vector.

Finally, combining Eq. 9 with Eq. 2 and Eq. 4, we can write the continuity equations for the wind-farm and upper layer as

$$\frac{1}{\rho_0}\frac{\partial p_1}{\partial t} + \frac{1}{\rho_0}\boldsymbol{U}_1 \cdot \nabla p_1 + H_1 \nabla \cdot \left[\mathcal{F}^{-1}\underline{\Phi}(\hat{\Phi}) * \boldsymbol{u}_1\right] = 0, \tag{12}$$

$$\frac{1}{\rho_0}\frac{\partial p_2}{\partial t} + \frac{1}{\rho_0}\boldsymbol{U}_2 \cdot \nabla p_2 + H_2 \nabla \cdot \left[\mathcal{F}^{-1}\underline{\Phi}(\hat{\Phi}) * \boldsymbol{u}_2\right] = 0 \tag{13}$$

where $p = p_1 + p_2$ is intended as the sum of the pressure perturbations induced by the vertical displacements η_1 and η_2, respectively. This form will be used in the remainder of the manuscript.

The three-layer model configuration described above has been validated against LES results by Allaerts and Meyers (2019) (see Section 3 VAL2) on a two dimensional (x-z) domain (i.e., all spanwise derivatives are set to zero). The model shows a mean absolute error (MAE) of 1.3% and 1.8% in terms of maximum displacement of the inversion layer and maximum pressure disturbance, respectively. Moreover, the model underestimates the velocity over the wind-farm area with a MAE of 5.6%. Note that the three-layer model is a linearized model, hence the discrepancies with LES results increase with increasing perturbation values. In fact, the model agrees very well with LES data when perturbations are small (i.e. when non-linear effects are negligible). For further details, we refer to Allaerts and Meyers (2019).

2.2 Optimization model

The goal of the optimization framework is to find a time-periodic optimal thrust-coefficient distribution $C_T^{\mathrm{O}}(x, y, t)$ that minimizes the gravity-wave induced blockage effects, maximizing the flow wind speed and consequently the wind-farm energy extraction over a selected time period T. The background atmospheric state ~~itself~~ is presumed to be steady~~.~~, which is the reason why we use a time-periodic control (i.e. leading to a moving time average of the optimal control that is steady, and does not lead to end-of-time effects). The wind-farm layout and the atmospheric state are inputs of the optimization model and are detailed in Section 3.

By using axial momentum theory (Burton et al., 2001), we find that the power coefficient $C_p(x, y, t)$ depends upon the thrust coefficient according to the following non-linear relationship

$$C_p = \frac{C_T}{2}\left(1 + \sqrt{1 - C_T}\right). \tag{14}$$

The objective function of the optimization model consists in the energy extracted by the farm in the time interval $[0,T]$, ~~and~~ hence it is defined as

$$\mathcal{J}(\boldsymbol{\psi},C_T) = -\beta\|\boldsymbol{U}_1\| \int_0^T \iint_\Omega C_p B(x,y)\left(\|\boldsymbol{U}_1\|^2 + 3\boldsymbol{U}_1\cdot\boldsymbol{u}_1\right) \mathrm{d}\boldsymbol{x}\mathrm{d}t \tag{15}$$

where $\Omega = D_x \times D_y$ is the computational domain area~~and $C_p(x,y,t)$ is the power coefficient distribution.By using axial momentum theory (Burton et al., 2001), we find that the power coefficient depends upon the thrust coefficient according to the following~~. The non-linear ~~relationship~~

$$C_p = \frac{C_T}{2}\left(1+\sqrt{1-C_T}\right),$$

~~so that the~~ relationship between C_p and C_T and the product between control and state variables in Eq. 15 imply that the objective function $\mathcal{J}$ is non-convex.

The wind-farm optimal configuration that maximizes the energy output (note that the objective function is defined with a minus sign) is then obtained by solving the following non-linear time-periodic PDE-constrained optimization problem

$$\min_{\boldsymbol{\psi},C_T} \quad \mathcal{J}(\boldsymbol{\psi},C_T) \tag{16}$$

s.t.

$$\begin{aligned}
&\frac{\partial \boldsymbol{u}_1}{\partial t} + \boldsymbol{U}_1\cdot\nabla\boldsymbol{u}_1 + \frac{1}{\rho_0}\nabla p_1 + \frac{1}{\rho_0}\nabla p_2 + f_c\boldsymbol{J}\cdot\boldsymbol{u}_1 - \nu_{t,1}\nabla^2\boldsymbol{u}_1 - \frac{\boldsymbol{D}'}{H_1}\cdot(\boldsymbol{u}_2-\boldsymbol{u}_1) + \frac{\boldsymbol{C}'}{H_1}\cdot\boldsymbol{u}_1 = \frac{\boldsymbol{f}^{(0)}+\boldsymbol{f}^{(1)}}{H_1} && \text{in } \Omega\times(0,T],\\
&\frac{\partial \boldsymbol{u}_2}{\partial t} + \boldsymbol{U}_2\cdot\nabla\boldsymbol{u}_2 + \frac{1}{\rho_0}\nabla p_1 + \frac{1}{\rho_0}\nabla p_2 + f_c\boldsymbol{J}\cdot\boldsymbol{u}_2 - \nu_{t,2}\nabla^2\boldsymbol{u}_2 + \frac{\boldsymbol{D}'}{H_2}\cdot(\boldsymbol{u}_2-\boldsymbol{u}_1) = 0 && \text{in } \Omega\times(0,T],\\
&\frac{1}{\rho_0}\frac{\partial p_1}{\partial t} + \frac{1}{\rho_0}\boldsymbol{U}_1\cdot\nabla p_1 + H_1\nabla\cdot\left[\mathcal{F}^{-1}\Phi(\hat{\Phi}) * \boldsymbol{u}_1\right] = 0 && \text{in } \Omega\times(0,T],\\
&\frac{1}{\rho_0}\frac{\partial p_2}{\partial t} + \frac{1}{\rho_0}\boldsymbol{U}_2\cdot\nabla p_2 + H_2\nabla\cdot\left[\mathcal{F}^{-1}\Phi(\hat{\Phi}) * \boldsymbol{u}_2\right] = 0 && \text{in } \Omega\times(0,T],\\
&0 \le C_T < 1 && \text{in } \Omega\times(0,T],\\
&C_T(x,y,0) = C_T(x,y,T) && \text{in } \Omega.
\end{aligned}$$

The constraints are the state (or forward) equations presented in the previous paragraph. Since Eq. 14 is defined only for $C_T \in [0,1)$, we added a box constraint to the optimization model. Moreover, the time-periodicity is imposed by assuming $C_T(x,y,0) = C_T(x,y,T)$. The system state $\boldsymbol{\psi} = \left[u_1, v_1, u_2, v_2, p_1, p_2\right]$ includes the velocity and pressure perturbations in the wind-farm and upper layer, which also define the unknowns of the three-layer model. The control parameters consist of the value of the thrust set point in each grid cell within the wind-farm area. Hence, the size of the control space is proportional to $N_x^{\mathrm{wf}} N_y^{\mathrm{wf}} N_t$, where N_t represents the number of time steps within the time horizon T, while N_x^{wf} and N_y^{wf} denote the number of grid points within the wind-farm area along the x and y-direction, respectively.

It is common practice in PDE-constrained optimization problem to not optimize the cost functional $\mathcal{J}(\boldsymbol{\psi},C_T)$ directly because such a problem would span both the state and control space. To avoid exploring the entire feasibility region, we

require $\boldsymbol{\psi}(C_T)$ to be the solution of the state equations throughout the optimization process. In other words, ~~if we use the shorthand notation~~ defining an operator $\mathcal{N}(\boldsymbol{\psi}, C_T)$ ~~for the state constraints~~that denotes the state equations, we are enforcing ~~that~~ $\mathcal{N}(\boldsymbol{\psi}(C_T), C_T) = 0$ during optimization iterations. This technique leads us to a reduced optimization problem with feasibility region given by the control space (De Los Reyes, 2015). The reduced optimization problem is written as

$$\min_{C_T} \quad \tilde{\mathcal{J}}(C_T) = \mathcal{J}\big(\boldsymbol{\psi}(C_T), C_T\big) \tag{17}$$

s.t.

$$\begin{aligned} &0 \le C_T < 1 && \text{in } \Omega \times (0,T], \\ &C_T(x,y,0) = C_T(x,y,T) && \text{in } \Omega \end{aligned}$$

where the only remaining constraints are the ones on the control parameters.

The gradient of the reduced objective function $\nabla\tilde{\mathcal{J}}$ is needed for the solution of the reduced optimization problem. To this end, we use ~~a~~ the continuous adjoint method. The adjoint (or backward) equations are given by (see Appendix A2 for detailed derivation)

$$\begin{aligned}
&-\frac{\partial \boldsymbol{\zeta}_1}{\partial t} - \boldsymbol{U}_1 \cdot \nabla \boldsymbol{\zeta}_1 + f_c \boldsymbol{J} \cdot \boldsymbol{\zeta}_1 - \nu_{t,1} \nabla^2 \boldsymbol{\zeta}_1 + \frac{\boldsymbol{D}'}{H_1} \cdot \boldsymbol{\zeta}_1 + \frac{\boldsymbol{C}'}{H_1} \cdot \boldsymbol{\zeta}_1 - \frac{\boldsymbol{D}'}{H_2} \cdot \boldsymbol{\zeta}_2 - H_1 \big[\mathcal{F}^{-1}(\Phi\hat{\Phi})(-\boldsymbol{x}, -t) * \nabla \Pi_1\big] + \\
&+ \frac{\beta}{H_1} \frac{C_T B(x,y)}{\|\boldsymbol{U}_1\|} \frac{\beta C_T B(x,y)}{H_1} \boldsymbol{U}_{1 1+1 2'} \cdot \boldsymbol{\zeta}_1 = 3\beta C_p B(x,y) \|\boldsymbol{U}_1\| \boldsymbol{U}_1 && \text{in } \Omega \times (0,T], \\
&-\frac{\partial \boldsymbol{\zeta}_2}{\partial t} - \boldsymbol{U}_2 \cdot \nabla \boldsymbol{\zeta}_2 + f_c \boldsymbol{J} \cdot \boldsymbol{\zeta}_2 - \nu_{t,2} \nabla^2 \boldsymbol{\zeta}_2 + \frac{\boldsymbol{D}'}{H_2} \cdot \boldsymbol{\zeta}_2 - \frac{\boldsymbol{D}'}{H_1} \cdot \boldsymbol{\zeta}_1 - H_2 \big[\mathcal{F}^{-1}(\Phi\hat{\Phi})(-\boldsymbol{x}, -t) * \nabla \Pi_2\big] = 0 && \text{in } \Omega \times (0,T], \\
&-\frac{\partial \Pi_1}{\partial t} - \boldsymbol{U}_1 \cdot \nabla \Pi_1 - \nabla \cdot \boldsymbol{\zeta}_1 - \nabla \cdot \boldsymbol{\zeta}_2 = 0 && \text{in } \Omega \times (0,T], \\
&-\frac{\partial \Pi_2}{\partial t} - \boldsymbol{U}_2 \cdot \nabla \Pi_2 - \nabla \cdot \boldsymbol{\zeta}_1 - \nabla \cdot \boldsymbol{\zeta}_2 = 0 && \text{in } \Omega \times (0,T].
\end{aligned} \tag{18}$$

Note that the minus sign in the argument of $\mathcal{F}^{-1}(\hat{\Phi})(-\boldsymbol{x}, -t)$ is not a result from classical integration by parts, but arrives from applying Fubini's theorem to the convolution term in Eq. 12 and Eq. 13 (see Appendix A2 for details). The adjoint variables are grouped in the vector $\boldsymbol{\psi}^* = [\boldsymbol{\zeta}_1, \boldsymbol{\zeta}_2, \Pi_1, \Pi_2]$ where $\boldsymbol{\zeta}_1 = (\zeta_1, \chi_1)$ and $\boldsymbol{\zeta}_2 = (\zeta_2, \chi_2)$ are the adjoint velocity perturbation fields in the wind-farm and upper layer, respectively, while Π_1 and Π_2 are the adjoint pressure perturbations. Using the solution of the adjoint equations, the gradient of the cost function is expressed as (see Appendix A3 for details)

$$\nabla\tilde{\mathcal{J}} = \beta B(x,y) \frac{\beta B(x,y)}{H_1} \left[\frac{1}{H_1} \|\boldsymbol{U}_1\| \boldsymbol{U}_1 \cdot \boldsymbol{\zeta}_1 - H_1 \|\boldsymbol{U}_1\| \frac{\mathrm{d}C_p}{\mathrm{d}C_T} \left(\|\boldsymbol{U}_1\|^2 + 3\boldsymbol{U}_1 \cdot \boldsymbol{u}_1 \right) + \frac{1}{H_1 \|\boldsymbol{U}_1\|} \boldsymbol{u}_1^\top \cdot \boldsymbol{U}_{1 1+1 2'} \cdot \boldsymbol{\zeta}_1 \right], \tag{19}$$

where $\mathrm{d}C_p/\mathrm{d}C_T$ is computed from Eq. 14. To compute the gradient $\nabla\tilde{\mathcal{J}}$ we need to solve the forward and backward equations. Since the cost for solving the adjoint ~~equation~~ equations is roughly the same as for the forward equation, the computational cost for evaluating $\nabla\tilde{\mathcal{J}}$ is proportional to the cost of solving twice the state equations. ~~A verification of~~ To verify the approach, ~~by comparing~~ we compare the adjoint gradient to a standard finite-difference approximation ~~, is presented~~ in Appendix A4.

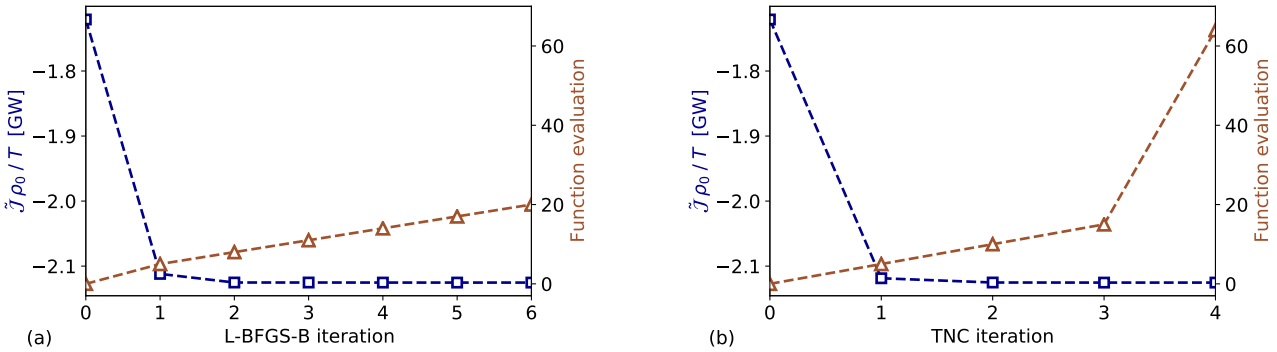

Figure 1. Convergence of the cost functional over the (a) L-BFGS-B and (b) TNC iteration. The squares and triangles denote the cost functional value and the number of function evaluations, respectively.

3 Numerical setup and case description

We define the model setup used to asses the potential of set-point optimization in mitigating self-induced gravity-wave effects in this section. We discuss the numerical setup in Section 3.1. Next, the selected wind-farm layout is presented in Section 3.2. Finally, the atmospheric state is discussed in Section 3.3.

3.1 Numerical setup

Both the forward and adjoint equations are discretized using a Fourier–Galerkin spectral method in space and time. The use of Fourier modes in time, automatically results in satisfying the periodicity conditions that we are aiming for in our optimization set-up. All terms in the equations are linear, besides the first-order term of the wind-farm drag force (and its adjoint). These terms contain products between temporarily and spatially dependent variables. To avoid expensive convolution sums, these products are computed in physical space. Full dealiasing is obtained by padding and truncation according to the 3/2 rule (Canuto et al., 1988). The use of Fourier modes in space forces periodic boundary conditions at the edges of the computational domain. Therefore, the domain has a sufficiently large dimension $D_x \times D_y = 1000 \times 400$ km^2, so that the perturbations die out before being recycled. The grid has $N_x \times N_y = 4000 \times 1600$ grid points which corresponds to a space resolution of ~~$\Delta x = \Delta y = 250$~~ $\Delta = 250$ m or 6.4×10^6 DOF per layer. Finally, different time horizon values are used spanning from $T = 10$ minutes to $T = 10$ hours with number of time steps ranging from $N_t = 12$ to $N_t = 120$. The discretized forward and backward equations form two systems of dimension $6N_xN_yN_t \times 6N_xN_yN_t$, which are solved using the LGMRES algorithm (Baker et al., 2005).

For the optimization, two different algorithms are compared in Fig. 1. The L-BFGS-B (limited-memory Broyden–Fletcher-Goldfarb–Shanno with box constraint) algorithm (Byrd et al., 1995) is an iterative quasi-Newton method. In the current application, the step length is evaluated with the inexact line search Wolfe condition (Wolfe, 1969). The truncated Newton method (TNC) computes the search direction by solving iteratively the Newton equation, applying the conjugate gradient method. This inner loop is stopped (truncated) as soon as a termination criterion is satisfied (Nocedal and Wright, 1999). In both cases, the

system matrix of the Newton equation consists of an approximate Hessian matrix, while the right-hand side needs gradient information to be computed, which are provided by the continuous adjoint method (see Appendix A for derivation and validation). Fig. 1 ~~(a) shows~~ shows that the cost function decreases rapidly in the firsts two to three algorithm iterations, reaching a plateau afterwards. The use of a quasi-Newton method in combination with the limited complexity of our optimization model (for instance, the constraints are linearized equations) allow us to reach such a fast convergence. Moreover, the continuous adjoint method limits the number of function evaluations, since it is not necessary to evaluate $\tilde{J}(C_T + \alpha\delta C_T)$ for all directions δC_T in the control space (at the expenses of solving an auxiliary set of equations). In particular, Fig. 1(a) displays that the cost functional is converged after six L-BFGS-B iterations. Apart from the first iteration, the line search method needs three 'function evaluations' before updating the cost functional. Hence, we need to solve 20 times the forward and backward equations for reaching convergence. On the other hand, Fig. 1(b) ~~shows~~ illustrates that the cost functional is mainly minimized within the first TNC iteration and convergence is reached after only four iterations. However, ~~here,~~ 63 function evaluations are needed. Hence, we will use the L-BFGS-B algorithm for solving the PDE-constrained optimization problem in the remainder of the article. To limit computational effort, a maximum of four L-BFGS-B iterations will be performed.

The solver (which is not parallelized) takes a couple of hours to solve the equations for a grid with resolution of 250 m (6.4×10^6 DOF per layer). Since convergence is reached after approximately 20 function evaluations (which means that we solve state and adjoint equations 20 times), the optimizer takes a couple of days to compute an optimal thrust set-point distribution. However, after this work was performed, we have upgraded the forward solver which is now 700 times faster than our previous version. Optimization of the backward solver is planned for the future, and we expect that this will lead to an optimization algorithm that will only take several minutes for the same case.

3.2 Wind-farm layout

We choose a wind-farm layout that resembles in size the Belgian-Dutch wind-farm offshore cluster located in the North Sea~~in size~~, but simplified to a rectangular shaped wind-farm with length $L_x = 20$ km and width $L_y = 30$ km. This choice also leads to a width-to-depth ratio of 3/2 which is known to be the ratio for which self-induced gravity-wave effects are maximum (Allaerts and Meyers, 2019). The wind turbine relative ~~spacing~~ spacings along the x- and y-direction are $s_x = s_y = 5.61$ (both non-dimensionalized with respect to the turbine rotor diameter D)~~. The turbine relative spacings are needed for computing the coefficient β (see Eq.8). Both~~ , so that the density of turbines in the farm is similar to the one of Allaerts and Meyers (2019) (i.e. leading to $\beta = 0.01$ in Eq. 8, setting both the wake efficiency η_w and γ ~~are assumed to be constant within the wind-farm area and are set to~~ to 0.9 ~~, similar to Allaerts and Meyers (2018).~~ as in Allaerts and Meyers (2018)). Note that we do not define a specific layout or a number of turbines but we only fix the density of turbines in the farm. The turbine dimensions are based on a DTU 10-MW IEA wind turbine (Bortolotti et al., 2019) with rotor diameter $D = 198$ m and turbine hub height $z_h = 119$ m.

3.3 Background state variables

The governing equations are linearized around a constant background state. To determine this state, we need vertical profiles of potential temperature, velocity, shear stress and eddy viscosity plus the surface roughness z_0 and the friction velocity u_*. We describe the techniques used in determining these profiles in the remainder of this section. Similar to Allaerts and Meyers (2019), we select two atmospheric states for initial testing ~~in Section 4.1~~of the optimizer, corresponding to ~~a subcritical and supercritical condition (see further below)~~sub- and supercritical flow conditions.

We choose a temperature profile that corresponds to a conventionally neutral ABL. The potential temperature in the neutral ABL is fixed to $\theta_0 = 288.15$ K. A capping inversion strength $\Delta\theta$ of 5.54 K and 3.7 K is used, which ~~will~~ lead to a sub- and supercritical flow, respectively (see below). Finally, a free atmosphere lapse rate $\Gamma = 1$ K/km is chosen. The lapse rate also defines the Brunt-Väisälä frequency N.

The velocity and stress profiles within the ABL are obtained following the approach of Nieuwstadt (1983). The non-dimensional surface roughness length $\overline{z}_0 = z_0/H$ and the non-dimensional boundary-layer height $h_* = Hf_c/u_*$ are the input parameters of Nieuwstadt's model, where f_c is the Coriolis frequency and $H = H_1 + H_2$ is the ABL height. The wind-farm layer height is assumed to be twice the turbine hub height, so $H_1 = 2z_h$. The ABL height is fixed to $H = 1000$ m and the friction velocity is set to $u_* = 0.6$ m/s. Finally, a surface roughness of $z_0 = 10^{-1}$ m is adopted. Using $h_* = 0.166$ and $\overline{z}_0 = 10^{-4}$ as input values for the Nieuwstadt's model, we derive the velocity $\boldsymbol{U}_1$, $\boldsymbol{U}_2$, the eddy viscosity $\nu_{t,1}$, $\nu_{t,2}$ for the wind-farm and upper layer and the friction coefficients C and D (used for computing the matrices $\boldsymbol{C}'$ and $\boldsymbol{D}'$, see Allaerts and Meyers (2019)). Besides the friction coefficients C and D which are given at $z = 0$ and $z = H_1$, all other physical quantities are depth-averaged over the height H_1 and H_2. Finally, the wind profile is oriented such that the wind in the wind-farm layer is always directed along the x-axis (i.e, $V_1 = 0$ m/s).

The pressure gradient strengths induced by inversion and internal gravity waves are dependent upon the Froude number $F_r = U_B/\sqrt{g'H}$ and a non-dimensional group $P_N = U_B^2/NH\|\boldsymbol{U}_g\|$, respectively (Smith, 2010; Allaerts and Meyers, 2019), where the velocity scale U_B is defined as

$$U_B = \left(\frac{H_1}{H}\frac{1}{U_1^2} + \frac{H_2}{H}\frac{1}{U_2^2}\right)^{\frac{1}{2}}. \tag{20}$$

The chosen background state defines a Froude number of 0.9 for $\Delta\theta = 5.54$ K, which implies subcritical flow conditions ($F_r < 1$), and a Froude number of 1.1 for $\Delta\theta = 3.7$ K, which leads to supercritical flow conditions ($F_r > 1$). Further, P_N expresses the impact of internal waves in the troposphere which increases when P_N decreases. The background state defined in Table 1 leads to $P_N = 1.92$. The numerical setup, wind-farm layout and background state variables are summarized in Table 1.

4 Results and discussion

We discuss the results of the optimization problem in the current section. Firstly, ~~in Section 4.1~~ the optimal thrust-coefficient distributions and relative energy gains are illustrated for two specific flow conditions ~~introduced in Section 3.3~~in Section 4.1. Thereafter, the sensitivity of the energy gain to the atmospheric state is studied in Section 4.2.

Table 1. Numerical setup, wind-farm layout and atmospheric state used in this manuscript.

Numerical setup	
Domain size	$D_x \times D_y = 1000 \times 400$ km^2
Grid size	$N_x \times N_y = 4000 \times 1600$
~~Cell size~~ Grid resolution	~~$\Delta_x \times \Delta_y = 250 \times 250$ m^2~~ $\Delta = 250$ m
Time horizon	Span from $T = 10$ min to $T = 10$ h
Time step	Span from $N_t = 12$ to $N_t = 120$
Discretization technique	Fourier–Galerkin
Equation solver	LGMRES
Optimization method	L-BFGS-B
L-BFGS-B iterations	$N_{it} = 4$
Wind-farm layout	
Wind-farm length	$L_x = 20$ km
Wind-farm width	$L_y = 30$ km
Turbine hub height	$z_h = 119$ m
Turbine rotor diameter	$D = 198$ m
Rated wind speed	$U_r = 11$ m/s
Relative turbine spacing	$s_x = s_y = 5.61$
Wake efficiency	$\eta_w = 0.9$
Velocity shape factor	$\gamma = 0.9$
Atmospheric state	
ABL potential temperature	$\theta_0 = 288.15$ K
Capping inversion strength	$\Delta\theta = 5.54$ K $\rightarrow F_r = 0.9$
	$\Delta\theta = 3.70$ K $\rightarrow F_r = 1.1$
Free atmosphere lapse rate	$\Gamma = 1$ K/km
Surface roughness	$z_0 = 10^{-1}$ m
Coriolis frequency	$f_c = 10^{-4}$ 1/s
Friction velocity	$u_* = 0.6$ m/s
Boundary layer height	$H = 1000$ m
Friction coefficients	$C = 3.76 \times 10^{-3}$
	$D = 1.51 \times 10^{-1}$

4.1 Optimal thrust-coefficient distributions

The optimization model described in Section 2.2 is time and space dependent. Hence, the model is capable of finding a time-periodic optimal thrust-coefficient distribution over the wind-farm area in a fixed time interval $[0, T]$. However, all optimal thrust set-point distributions found for the different combinations of time horizons and time steps reported in Table ~~1~~1, are constant in time. We have verified this using a range of steady and unsteady starting conditions for C_T in the algorithm, but did not find any unsteady ~~optimums. Therefore, we~~ optimum. We believe that this is due to two reasons. Firstly, we use steady-state inflow conditions, therefore neglecting meso-scale temporal variations in the velocity field (these could lead to time-dependent optimal control signals, but are not included in the current work). Secondly, the objective function is non-convex and there is no proof about the uniqueness of global minima. Hence, there is no guarantee that the optimal solution found by the optimizer corresponds to a global optimum. Nevertheless, since we do not observe any unsteady behaviour in our optimal solutions, we show only steady-state results in the remainder of the manuscript, and conclude for the time being that unsteady time-periodic excitation is less effective than a stationary spatially optimal distribution in this context.

We also note that our findings are in contrast with recent works of Goit and Meyers (2015), Munters and Meyers (2018) and Frederik et al. (2020), in which the authors illustrated the benefits of dynamic induction control over yaw and static induction control. However, the characteristic time scale of gravity-wave effects is estimated to be approximately 1 h (Gill 1982, Allaerts and Meyers 2019) which is an order of magnitude above the typical time scale of wake convection between turbines, and turbulent mixing in turbine wakes (this also justifies the larger sampling time used). Hence, while unsteadiness of the thrust coefficient (with a typical time scale of 50 seconds for large scale turbines) can lead to improved wake mixing (Goit and Meyers, 2015; Munters and Meyers, 2018; Frederik et al., 2020), it has no impact on phenomena that occur at larger time scales, such as wind-farm induced gravity waves.

The steady-state optimal thrust-coefficient distributions obtained in sub- and supercritical conditions are analyzed in the remainder of this section. To improve the understanding of such distributions, gravity-wave induced flow patterns obtained with $C_T^{\mathrm{O}}(x, y)$ are compared with a reference case. The setup of the reference model is the one reported in Table 1 but instead a uniform thrust set-point distribution over the wind-farm area is used, with $C_T^{\mathrm{R}}(x, y) = C_T^{\mathrm{Betz}} = 8/9$.

Fig. 2 illustrates a top view of the perturbation flow patterns obtained with $F_r = 0.9$ (top row) and $F_r = 1.1$ (bottom row) using the reference model setup. The farm extracts energy from the flow, causing a momentum sink in the wind-farm layer. Due to the continuity constraint, an upward flow displacement above the wind-farm area takes place which causes the boundary layer height to increase. Fig. 2(a) shows for the subcritical case, that an inversion-layer vertical displacement of about 65 meter takes place at the wind-farm entrance region. A second peak of lower magnitude is located in the downwind region. On the other hand, for the supercritical case, Fig. 2(d) displays a similar maximum value of η_t attained close to the wind-farm center. In both cases, the inversion-layer vertical displacement decreases in the wind-farm exit region and assumes a wavy behaviour in the wind-farm wake. The vertical displacement of air parcels triggers inversion waves on the 2D inversion layer surface and internal waves in the free atmosphere (3D waves). These waves induce pressure gradients, as visible in Fig. 2(b,e), where a region of high pressure builds up in correspondence with high η_t values, leading to flow blockage. However, Fig. 2(b) shows a stronger

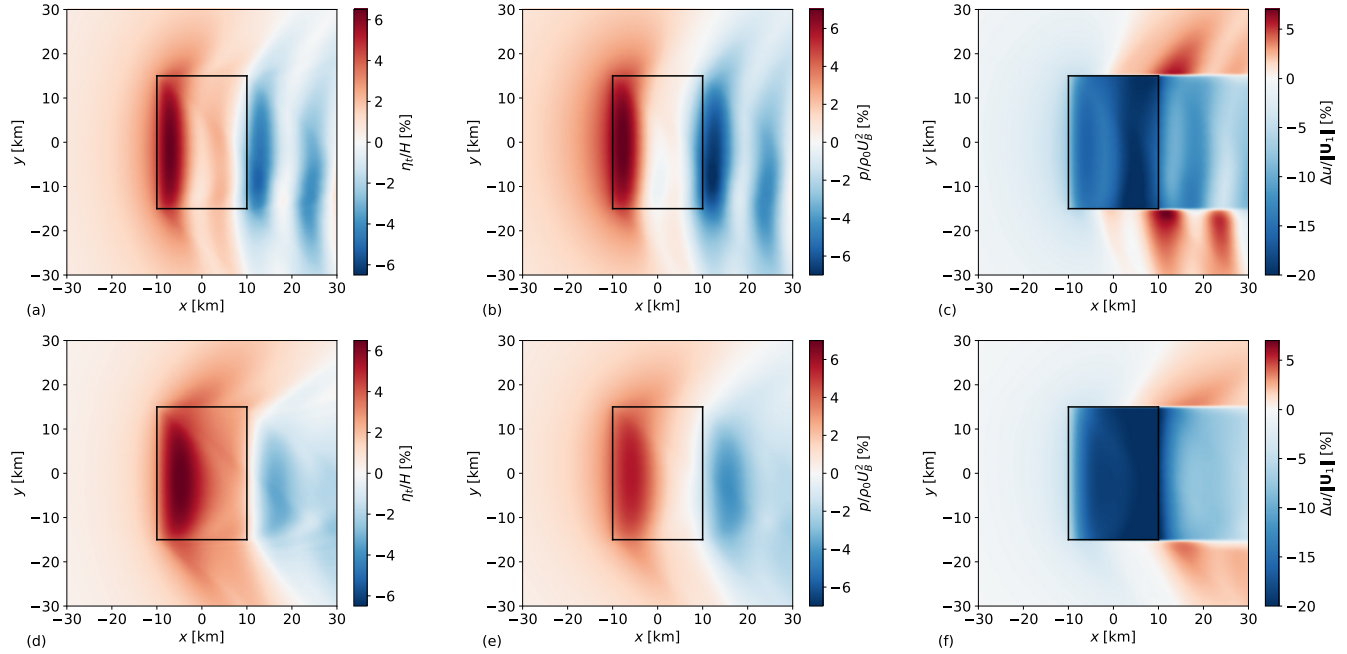

Figure 2. Planform view of inversion-layer displacement (a,d), pressure perturbation (b,e) and relative velocity reduction (c,f) in the wind-farm layer in subcritical (top row, $F_r = 0.9$) and supercritical (bottom row, $F_r = 1.1$) flow conditions. The black rectangle indicates the wind-farm region.

adverse pressure gradient in the wind-farm induction region than the one in Fig. 2(e). In fact, inversion waves travel upstream in subcritical conditions, which leads to more slow-down in the induction region. In both sub- and supercritical case, favourable pressure gradients ~~develop within the wind-farm area which tend to accelerate the flow in the wind-farm exit region~~reduce the velocity deficits in the bulk of the farm. Finally, Fig. 2(c,f) illustrate relative velocity reductions in the wind-farm layer. The stronger inversion strength found in the subcritical flow case transforms the inversion layer in a quasi-rigid lid, which limits vertical displacements. The lower streamlines divergence over the wind-farm area implies lower velocity reductions. Moreover, the favourable pressure gradient is stronger when $F_r = 0.9$, allowing for ~~higher flow wind speeds~~ lower velocity deficits within the wind-farm area. This explains the higher velocity reduction (up to 20%) seen in Fig. 2(f). Such a strong response could be on the limit of our small amplitude assumption. The planform view of pressure and velocity perturbations in the wind-farm and upper layer in subcritical flow conditions are also illustrated on a wider domain in Appendix A (see Fig. A1).

The goal of our study is to find an optimal set-point distribution which reduces the velocity perturbations displayed in Fig. 2(c,f). While maximizing the flow wind speed through the farm, we also maximize the wind-farm energy extraction. To this end, we solve the optimization problem discussed in Section 2.2. The inputs of the optimization model are the wind-farm layout and the atmospheric conditions, which are detailed in Table 1. Moreover, an initial thrust-coefficient distribution needs to be specified. We have verified that for many different initial conditions the algorithm converges always to the same optimal

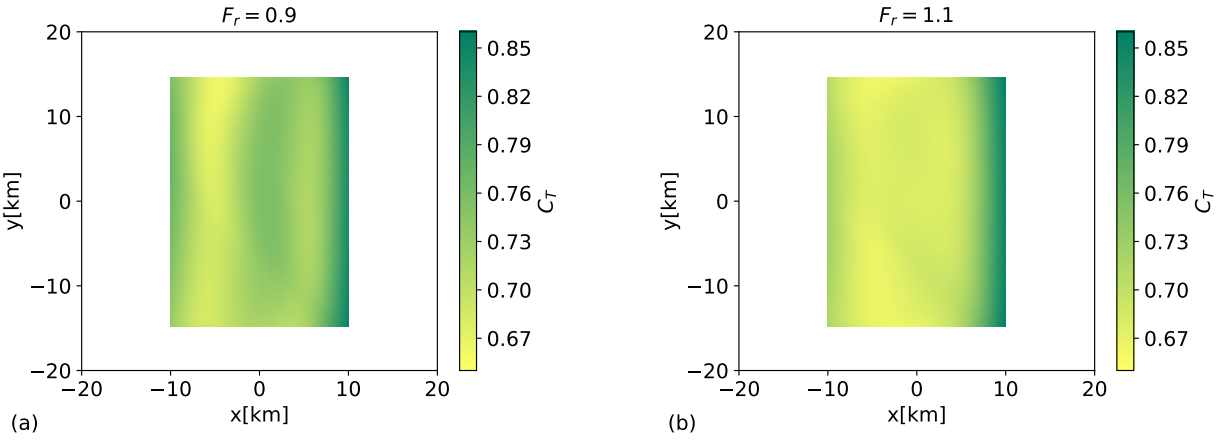

Figure 3. Planform view of (a) optimal thrust-coefficient distribution in subcritical ($F_r = 0.9$) and (b) supercritical flow conditions ($F_r = 1.1$). The length and width of the wind farm are 20 and 30 km, respectively.

solution. Therefore, a random initial thrust set-point distribution is chosen. The optimal configurations obtained for different Froude numbers are illustrated in Fig. 3. We find that the optimal thrust-coefficient distributions are non-uniform in space and assume different spatial distributions according to the atmospheric state. In particular, when the flow is subcritical the optimal thrust set-point distribution assumes a sinusoidal behaviour in the streamwise direction while it becomes a U-shaped curve when the flow is supercritical. In both cases, C_T^{O} is almost invariant along the spanwise direction.

We denote with $\tilde{\mathcal{J}}^{\mathrm{R}}$ and $\tilde{\mathcal{J}}^{\mathrm{O}}$ the energy extracted using $C_T = C_T^{\mathrm{R}} = 8/9$ and $C_T = C_T^{\mathrm{O}}$, respectively. Further, we define

$$\mathcal{G} = \frac{\tilde{\mathcal{J}}^{\mathrm{O}} - \tilde{\mathcal{J}}^{\mathrm{R}}}{\tilde{\mathcal{J}}^{\mathrm{R}}} \tag{21}$$

where $\mathcal{G}$ denotes the relative energy gain obtained using an optimal thrust-coefficient distribution instead of the reference one. The energy gains attained in sub- and supercritical flow conditions are 5.3% and 7%, respectively. Clearly, energy gains are also strongly dependent on the atmospheric conditions. Therefore, a sensitivity study is carried out in Section 4.2. To asses the benefit of an optimal non-uniform distribution over an optimal uniform one, we have applied the optimization framework developed in section 2.2 assuming a spatially invariant C_T. Results are discussed in Appendix B.

The optimal set-point distributions displayed in Fig. 3 are related to the vertical displacement of the inversion layer over the wind-farm area. Fig. 4 shows streamwise profiles of η_t and C_T^{O} through the center of the farm for $F_r = 0.9$ and $F_r = 1.1$. ~~The maximum value of η_t is similar for both the sub- and supercritical case, although the profiles differ considerably.~~ To reduce gravity-wave excitation, C_T^{O} is seen to be inversely related with η_t. ~~Moreover~~In fact, Fig. 4(a) shows that the streamwise profile of η_t has a sinusoidal behaviour. Hence, the optimal set-point distribution is sinusoidal as well, explaining the pattern displayed in Fig. 3(a). On the other hand, η_t assumes a U-shaped profile through the wind farm in supercritical conditions (see Fig. 4(b)), a profile that is also found in C_T^{O} (see Fig. 3(b)). Moreover, Fig. 2(a,d) show that the gradient of η_t along the spanwise direction is much smaller than the one along the streamwise direction, explaining the almost constant thrust set-

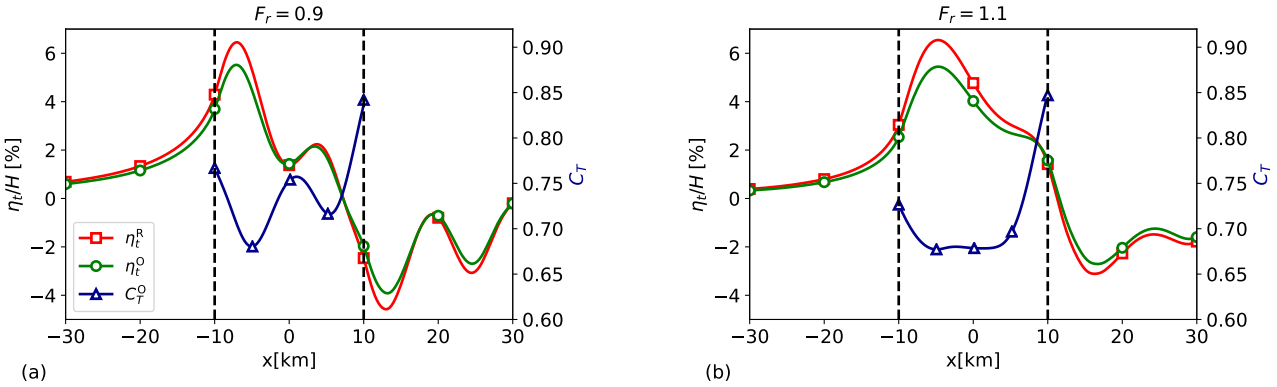

Figure 4. Streamwise profiles of optimal thrust set-point distribution (C_T^{O}), reference (η_t^{R}) and optimal (η_t^{O}) inversion-layer displacement in (a) subcritical ($F_r = 0.9$) and (b) supercritical flow conditions ($F_r = 1.1$). The wind-farm region is marked by vertical dashed lines, and the profiles have been obtained through the centre of the farm ($y = 0$).

point distributions along the y-direction. Fig. 4 also shows that ~~$\eta_{t,\max}^{\mathrm{R}} > \eta_{t,\max}^{\mathrm{O}}$~~ $\eta_{t,\max}^{\mathrm{O}} < \eta_{t,\max}^{\mathrm{R}}$ in both sub- and supercritical conditions, meaning that the optimal thrust set-point distribution decreases the upward flow displacement over the wind-farm area. The maximum inversion-layer displacement is located at the entrance region of the farm. If we compare η_t^{R} and η_t^{O} in this region, a displacement reduction of 14.5% and 16.8% is attained with the optimal configuration for the sub- and supercritical case, respectively.

A lower vertical displacement of the inversion layer reduces gravity-wave excitation, therefore we also expect a lower strength of the adverse pressure gradient at the entrance of the farm compared to the one obtained with C_T^{R}. Fig. 5(a,c) confirm this hypothesis, showing streamwise profiles of pressure perturbations p^{R} and p^{O} through the center of the farm for $F_r = 0.9$ and $F_r = 1.1$. The pressure peak is located at the entrance of the farm and a pressure peak reduction of 14.3% and 16.2% is attained with the optimal configuration for the sub- and supercritical case, respectively. Fig. 5(b,d) show streamwise profiles of velocity perturbations u_1^{R} and u_1^{O} through the center of the farm for $F_r = 0.9$ and $F_r = 1.1$. The lower adverse pressure gradient strength ~~in~~ attained with the optimal configuration allows for a lower velocity perturbation u_1 in the induction region with respect to the reference case. Moreover, the optimal configuration also reduces the streamline divergence, accounting for higher flow wind speeds through the farm. Consequently, a velocity perturbation reduction of 13.4% and 15.5% is attained for the sub- and supercritical case~~. Since the energy varies with the velocity cube, the higher velocity gain obtained in supercritical conditions with respect to the subcritical ones~~ , which explains the higher energy gain ~~attained~~obtained for $F_r = 1.1$.

The optimal thrust-coefficient distributions and energy gains discussed in this section are obtained with data listed in Table 1. However, the atmospheric state changes in real case scenarios and we have seen that the optimal configuration strongly depends upon the atmospheric parameters. Therefore, the sensitivity of the energy gain to the atmospheric state is performed in the next section.

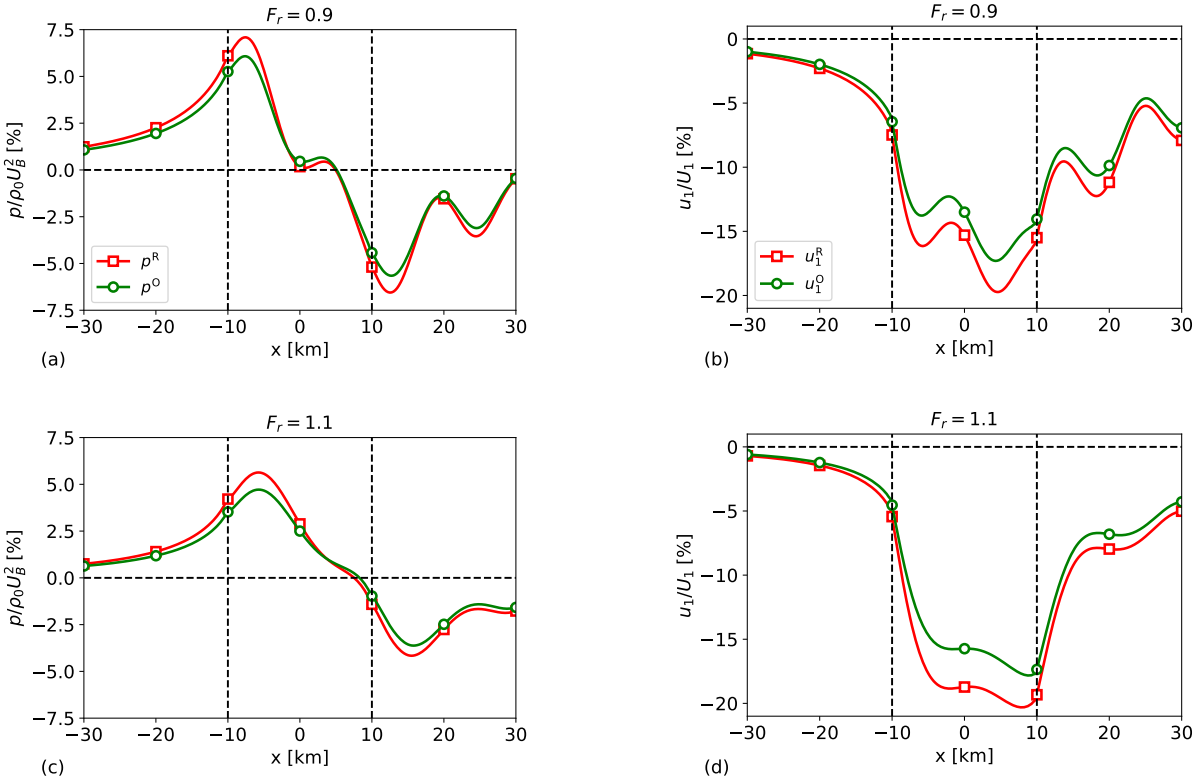

Figure 5. Streamwise profiles of (a,c) reference (p^{R}) and optimal (p^{O}) pressure perturbation and (b,d) reference (u_1^{R}) and optimal (u_1^{O}) velocity perturbation in subcritical (top row, $F_r = 0.9$) and supercritical (bottom row, $F_r = 1.1$) flow conditions. The wind-farm region is marked by vertical dashed lines, and the profiles have been obtained through the centre of the farm ($y = 0$).

4.2 Sensitivity study

Allaerts and Meyers (2019) pointed out that gravity-wave induced power loss is significant only for certain atmospheric states. Since our aim is to recover its power loss, we also expect the energy gain to be sensitive to the atmospheric conditions. We note that gravity-wave patterns are also sensitive to the wind-farm layout. However, a sensitivity study over the wind-farm layout is beyond the scope of the article.

The nondimensionalization of the three-layer model equations with respect to the boundary layer height H and the friction velocity u_* highlights four non-dimensional groups that govern the atmospheric state, which are:

- The non-dimensional boundary layer height $h_* = H f_c / u_*$. Values of $h_* \approx 0.1$ denote shallow boundary layers typically found over sea, while $h_* \approx 0.35$ rather relates to a deep land-based boundary layer. We vary h_* between 0.16 and 0.4;
- The non-dimensional surface roughness length $\overline{z}_0 = z_0/H$. This number varies on several order of magnitude according to the sea state or land surface. We vary $\log_{10}(\overline{z}_0)$ between -4.2 and -2.8 in the current study;

– The non-dimensional Brunt-Väisälä frequency N/f_c. The Brunt-Väisälä frequency is an important parameter in gravity-wave theory which expresses the highest possible frequency for internal gravity waves (Gill, 1982). Typical values of free atmosphere lapse rate Γ range between 1 and 10 K/km. Low and high Γ values are associated with weakly and strongly stratified atmospheres, respectively. We vary Γ between 0.03 and 12 K/km corresponding to $10 \leq N/f_c \leq 200$;

– The inversion parameter $g'H/Au_*^2$. According to Csanady (1974), the height of the inversion layer is determined by a balance of surface stress and buoyancy. Equilibrium conditions are reached when $g'H/Au_*^2 \approx 1$, with $A = 500$ being an empirical constant. We vary the inversion parameter between 0.5 and 1.5.

Allaerts and Meyers (2019) conducted a similar sensitivity study on the gravity-wave induced power loss on a wider range of non-dimensional numbers. However, since we are optimizing turbine thrust set points, we need to ensure that $U_1/U_r < 1$ ($U_r = 11$ m/s is the rated wind speed of the DTU 10 MW IEA wind turbine), otherwise turbines would operate in above-rated wind speed regime and it would not make any sense to optimize their power production. The choice of the four ranges for the non-dimensional groups discussed above ensures that $U_1/U_r \leq 0.9$ for all atmospheric states.

Using the atmospheric state reported in Table 1, the non-dimensional numbers assume values $h_* = 0.166$, $\overline{z}_0 = 10^{-4}$ and $N/f_c = 58$. The inversion parameter is equal to 1.046 and 0.691 in the sub- and supercritical case, respectively. The optimal thrust-coefficient distributions discussed in Section 4.1 were obtained using these dimensionless group values. The sensitivity of the energy gain to atmospheric conditions is performed by varying h_*, $\overline{z}_0$ and N/f_c against the inversion parameter $g'H/Au_*^2$, similarly to Allaerts and Meyers (2019). The numerical setup is the one detailed in Table 1. However, we use a grid cell size which is four times bigger ($\Delta x \times \Delta y = 1000 \times 1000$ m^2), meaning that we use 4×10^5 cells instead of 6.4×10^6, so that the necessary computational resources remain reasonable. To assess the validity of this choice, we performed a grid sensitivity study in Appendix C showing that the energy gain value changes of about 1% when the number of grid cells is increased of one order of magnitude (see Fig. C1). The high computational efficiency of the three-layer model allowed us to perform a sensitivity study of the optimization results over 1960 different atmospheric conditions (thus effectively running an optimization problem for every atmospheric ~~condition~~state). Since the wind-farm layout impact on energy gains is beyond the scope of our study, we impose the wind direction to be along the x-axis in the wind-farm layer in all simulations ($V_1 = 0$ m/s).

To better understand the energy gain sensitivity to atmospheric conditions, we examine how the non-dimensional parameters F_r and P_N impact the flow fields. The pressure gradients induced by inversion waves scale with g', therefore high inversion strengths correspond to strong inversion-wave feedback and low Froude number values. These two-dimensional waves are ~~nondispervive~~ non-dispersive with phase speed $\sqrt{g'H}$ (Sutherland, 2010). Therefore, F_r also represents the ratio of the bulk wind speed within the ABL to the velocity of the inversion waves. If $F_r < 1$ (subcritical flow) the two-dimensional waves can affect the upstream flow, while they can travel only downstream if $F_r > 1$ (supercritical flow). The flow is said to be critical when $F_r = 1$. On the other hand, internal-wave induced pressure gradients are governed by the second non-dimensional group P_N. Strong internal-wave feedback correspond to low P_N values. In fact, strongly stratified atmospheres imply high N values, meaning that they account for higher internal-wave oscillation frequencies and phase speed (Sutherland, 2010).

Two different flow regimes can be identified:

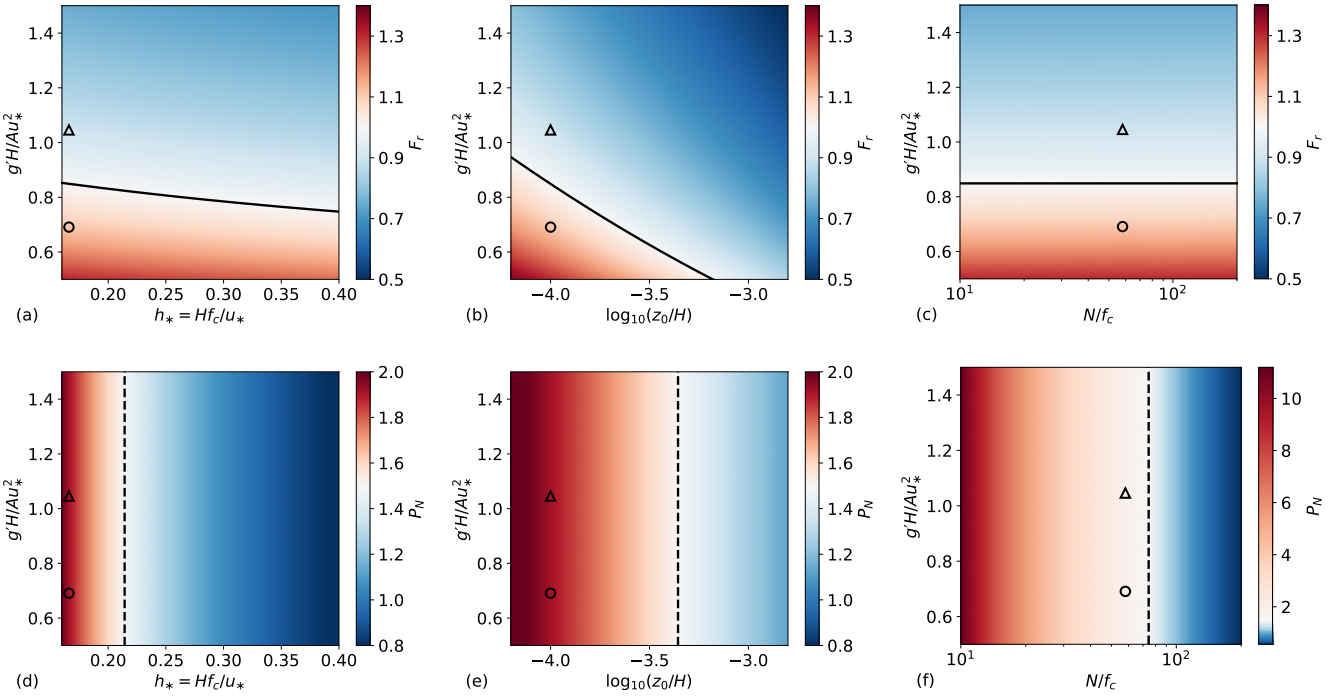

Figure 6. Sensitivity of (a-c) Froude number $F_r = U_B/\sqrt{g'H}$ and (d-f) $P_N = U_B^2/NH\|\boldsymbol{U}_g\|$ to atmospheric conditions. (a,d) Non-dimensional boundary layer height h_* (with $\overline{z}_0 = 10^{-4}$ and $N/f_c = 58$), (b,d) logarithm of the non-dimensional surface roughness length $\overline{z}_0$ (with $h_* = 0.166$ and $N/f_c = 58$) and (c,f) ratio of Brunt-Väisälä frequency to Coriolis parameter N/f_c (with $h_* = 0.166$ and $\overline{z}_0 = 10^{-4}$) against the inversion parameter $g'H/Au_*^2$. The black solid lines in (a-c) corresponds to critical flow conditions ($F_r = 1$) while the dashed black ones in (d-f) corresponds to flow conditions of $P_N = 1.5$. The markers △ and ○ represent the sub- and supercritical flow case studied in Section 4.1, respectively. Note that Fig. (f) use a different scale than Fig. (d,e).

- Regime 1: low P_N. The strongly stratified free atmosphere limits vertical displacement of air parcels, hence reduced streamline divergence over the wind-farm area is observed. This results in low velocity reductions and η_t values. Moreover, the flow fields are F_r-independent in these atmospheric states (Smith, 2010).

- Regime 2: high P_N. The inversion-layer strength determines the flow fields properties since the influence of internal waves is negligible. The weakly stratified atmosphere makes the ABL to behave like an idealized shallow-water system for $F_r \simeq 1$ (choking effect (Smith, 2010)). Moreover, the perturbations magnitude are strongly dependent upon the Froude number.

Smith (2010) and Allaerts and Meyers (2019) defined a third regime where $N = 0$ and $g' = 0$, which would correspond to $F_r, P_N \to \infty$ or to a purely neutral atmosphere. Gravity waves are not excited in this particular flow condition and only drag forces and frictional effects play a role in the flow behaviour. Since we are interested in finding optimal thrust set-point distributions which allow to recover gravity-wave induced power loss, we did not investigate this regime in the current study.

Fig. 6(a-c) illustrate the sensitivity of F_r to changes in h_*, $\overline{z}_0$ and N/f_c against the inversion parameter. In all cases, the Froude number ranges from approximatively 0.5 to 1.4. The black line denotes critical flow conditions. Lines of constant Froude number run parallel to this line, meaning that F_r is invariant and quasi-invariant to N/f_c and h_*, respectively. On the other hand, changes in $\overline{z}_0$ have a strong impact on the wind profile convexity and therefore on F_r. The sensitivity of P_N to the atmospheric state is displayed in Fig. 6(d-f). P_N is not dependent on the inversion parameter. Hence, lines of constant P_N values are vertical and parallel to the dashed black line, which denotes atmospheric conditions for which $P_N = 1.5$. This line divides the domain in regions where the internal-wave effects are important (regime 1, right side) or limited (regime 2, left side). However, internal waves still play a crucial role in softening the flow perturbations magnitude when P_N values are only slightly greater than 1, as in Fig. 6(d,e). On the other hand, very high P_N numbers ($P_N > 10$) are attained in weakly stratified conditions (see Fig. 6(f)). We will use the above mentioned regimes classification as a proxy for the interpretation of the energy gain sensitivity patterns (note that the term high and low in the regimes characterization are referred to the maximum and minimum F_r and P_N values found over the sensitivity domain).

Fig. 7(a-c) and Fig. 7(d-f) illustrate the sensitivity of the optimal inversion-layer vertical-displacement reduction $\mathcal{G}_\eta$, and energy gain $\mathcal{G}$ to changes in h_*, $\overline{z}_0$ and N/f_c, against the inversion parameter. The displacement reduction is defined as

$$\mathcal{G}_\eta = \left| \frac{\eta^{\mathrm{O}}_{t,\max} - \eta^{\mathrm{R}}_{t,\max}}{\eta^{\mathrm{R}}_{t,\max}} \right| \tag{22}$$

where $\eta^{\mathrm{O}}_{t,\max}$ and $\eta^{\mathrm{R}}_{t,\max}$ denote the maximum inversion-layer displacement attained with the optimal and reference model configuration, respectively. As we discussed in Section 4.1, the lowering of the inversion-layer vertical displacement reduces the strength of the adverse pressure gradient, increasing the flow wind speed and consequently the wind-farm energy output. Fig. 7 confirms this ~~state~~statement. In fact, regions of high vertical displacement reduction strictly correspond to regions of high energy gain.

Allaerts and Meyers (2017, 2018, 2019) found that for low ABL heights, gravity waves induce strong pressure gradients and play an important role in the distribution of the kinetic energy within the farm. Indeed, the large geostrophic wind angle found in shallow boundary layers redirects the favourable pressure gradient seen over the wind-farm area of 90 degrees for $h_* \to 0$, decreasing the dispersive impact of internal gravity waves. Fig. 7(d) displays that the maximum energy gain is indeed attained for $h_* = 0.17$ (i.e., for shallow boundary layer) in supercritical flow conditions, with gains of about 7.5% in correspondence to a displacement reduction of 17.5%. A similar pattern is seen in Fig. 7(e), where a maximum energy gain of 8.4% is attained again in supercritical conditions for $\log_{10}(\overline{z}_0) = -4.2$, in correspondence to a displacement reduction of 19%. Both $\mathcal{G}$ and $\mathcal{G}_\eta$ show higher sensitivity to changes in $\overline{z}_0$ than in h_*, decreasing rapidly for increasing value of surface roughness. Interestingly, energy gains are close to zero in case of high $\overline{z}_0$ values. This is due to the additional frictional drag which dissipates perturbation energy, limiting gravity-wave excitation and consequently the potential of our optimization.

The sensitivity of $\mathcal{G}$ and $\mathcal{G}_\eta$ to changes in free atmosphere stability are shown in Fig. 7(c,f). The high P_N sensitivity to changes in N (from $P_N \approx 11$ to $P_N \approx 0.5$ for increasing values of N/f_c) accounts for a clear distinction between regime 1 and regime 2. The former shows energy gains of about 5% while the latter attains gains of 14% in correspondence to inversion displacement reductions of 24%. Fig. 7(f) illustrates that the energy gain peak is obtained in critical flow conditions ($F_r = 1$),

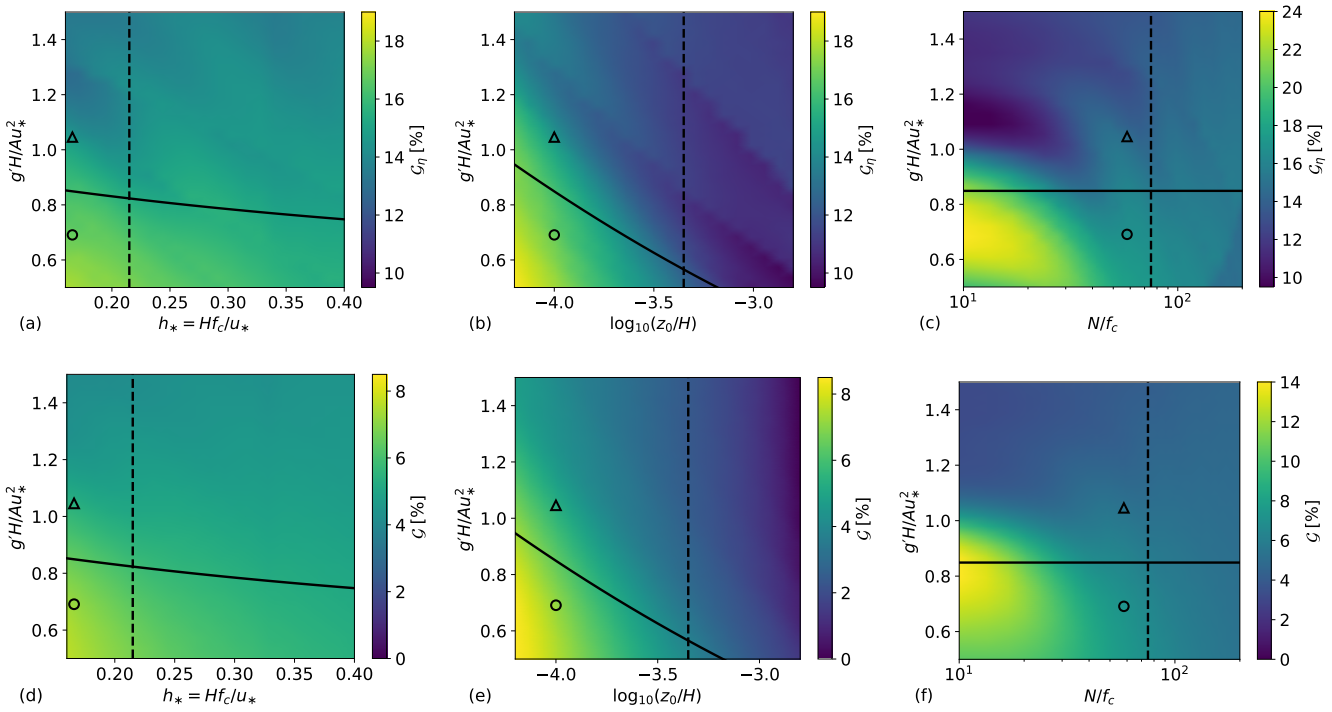

Figure 7. Sensitivity of (a-c) inversion-layer vertical-displacement reduction $\mathcal{G}_\eta$ and (d-f) energy gain $\mathcal{G}$ to atmospheric conditions. (a,d) Non-dimensional boundary layer height h_* (with $\overline{z}_0 = 10^{-4}$ and $N/f_c = 58$), (b,d) logarithm of the non-dimensional surface roughness length $\overline{z}_0$ (with $h_* = 0.166$ and $N/f_c = 58$) and (c,f) ratio of Brunt-Väisälä frequency to Coriolis parameter N/f_c (with $h_* = 0.166$ and $\overline{z}_0 = 10^{-4}$) against the inversion parameter $g'H/Au_*^2$. The black solid line corresponds to critical flow conditions ($F_r = 1$) while the black dashed line corresponds to flow conditions of $P_N = 1.5$. The markers $\triangle$ and $\circ$ represent the sub- and supercritical flow case studied in Section 4.1, respectively. Note that Figs. (c) and (f) use a different scale than Figs. (a,b) and (d,e).

differently from the previous cases. The very high P_N values (hence, the limited presence of internal waves) attained in correspondence to $F_r = 1$ allow for the choking effect to take place (Smith, 2010; Allaerts and Meyers, 2019). Very large flow perturbations are triggered in these atmospheric conditions, leaving greater potential for energy recovery. The choking effect is not ~~present~~ visible in Fig. 7(d,e), since there $P_N \approx 2$ when $F_r = 1$ (the flow perturbations are softened by internal waves).

Overall, higher inversion-layer displacement reductions and energy gains are attained in critical and supercritical flow conditions for high P_N values (regime 2), that is for low h_*, $\overline{z}_0$ and N/f_c. This is not surprising due to the strong impact that gravity waves have on farm's performance in such conditions (see Section 4.1 or Smith (2010) and Allaerts and Meyers (2019)). Moreover, we observe strong gradients of $\mathcal{G}$ and $\mathcal{G}_\eta$ along contours of P_N in regime 2, and weak gradients in regime 1. This suggests that the flow properties are F_r-independent for low P_N values, confirming the observations of Smith (2010).

5 Conclusions

In the current study, we investigated for the first time the potential of thrust set-point optimization in large wind farms for mitigating gravity-wave induced blockage effects, with the aim of increasing the wind-farm energy extraction. Thus, a fast boundary layer model proposed by Allaerts and Meyers (2019) was adopted. The three-layer model simulates the atmospheric response to turbine drag in large wind farms by dividing the vertical structure of the atmosphere into three layers. This approach accurately captures the effects of regional pressure gradients induced by large wind farms at low computational expenses. We first added the time-dependency to the model so that time-periodic gravity-wave patterns could be reproduced. Further, we reformulated the model as an optimization framework with the objective of maximizing the wind-farm energy output at all costs. Gradient information was derived using ~~a~~ the continuous adjoint method. To limit the computational cost, a ~~simple~~ box-function wind-farm force model was used which assumes that the force is distributed over the whole wind-farm area. ~~Hence, turbine-wake effects were not analytically resolved.~~ The wind-farm layout was inspired by the works of Allaerts et al. (2018) and Allaerts and Meyers (2019), roughly representing the Belgian–Dutch offshore wind-farm cluster.

The optimization model was applied to two different atmospheric states representative of subcritical ($F_r = 0.9$) and supercritical ($F_r = 1.1$) flow conditions. The optimal configurations were then compared with a reference model setup which uses a uniform thrust-coefficient distribution. We did not observe dynamic behaviour in the optimal thrust set-point distributions for different choices of time horizon and time step, meaning that it is not necessary to excite non-stationary wave patterns to further increase the wind-farm energy output. However, we observed interesting spatial patterns. The optimal thrust set-point distributions turned out to be inversely related with the inversion-layer vertical displacement η_t. This has led to a sinusoidal and U-shaped C_T^{O} distribution along the streamwise direction in sub- and supercritical conditions, respectively. An inversion-layer displacement reduction of 14.5% and 16.8% was observed in sub- and supercritical conditions, which lowered the adverse pressure gradient strength in the wind-farm induction and entrance region. The reduced blockage effects allowed for higher flow wind speeds through the farm. The optimal configurations showed energy gains of 5.3% and 7% in sub- and supercritical conditions with respect to the reference model setup.

The atmospheric state is far from being constant in real case scenarios, therefore the energy gain sensitivity to changes in atmospheric conditions was further studied. Thus, the developed thrust set-point optimization tool was applied for several wind profiles, inversion strengths and atmosphere stratifications for a total of 1960 different atmospheric states. Regions of high inversion-layer-displacement reduction in the sensitivity domain strictly corresponded to regions of high energy gain. This has confirmed that it is essential to reduce the streamline divergence over the wind-farm area for limiting gravity-wave induced power loss. The strong gravity-wave feedback in high P_N conditions made these atmospheric states the most suitable for energy recovery purposes. Energy gains up to 14% were found for weakly stratified atmospheres ($P_N \approx 11$) in correspondence of critical flow conditions ($F_r = 1$). This is related to the large flow perturbations induced by the chocking effect (Smith, 2010). Overall, energy gains above 4% were observed for 77% of the cases.

The results discussed in the current manuscript make wind-farm set-point optimization a promising tool for gravity-wave induced power loss recovery. However, many challenges remain before this can be translated to real wind-farm applications.

First of all, the wind-farm force model needs to be improved. The analytical wake model developed by Niayifar and Porté-Agel (2016) and used by Allaerts and Meyers (2019) could be adopted for ~~including turbine-wake effects in the optimization framework. Further~~having a more accurate and realistic representation of the forcing term. Furthermore, gravity-wave induced pressure gradient effects on turbine wakes recovery could be included using the model proposed by Shamsoddin and Porté-Agel (2018). This would allow us to optimize the turbine thrust set point of individual wind turbine placed in large wind farms. However, the complexity of the adjoint equations and the computational time will increase considerably. Moreover, the three-layer model has been validate with LES results only (Allaerts and Meyers (2019)). A more extensive validation of the model is topic for further research. In the future, we also plan to apply the results obtained in this article to a higher fidelity model (i.e, our in-house LES solver SP-Wind). However, this requires some work on the efficiency of non-reflecting boundary conditions in our LES solver (Allaerts and Meyers, 2017, 2018). Finally, we assumed that the free atmosphere is uniformly stratified, and steady. The relaxation of these assumptions would extend the applicability of the model, e.g, to atmospheres with height-dependent Brunt-Väisälä frequency, and geostrophic wind, among others.

Appendix A: Derivation and verification of the adjoint equations and the adjoint gradient

The continuous adjoint method is briefly explained in Appendix A1. Next, the three-layer model adjoint equations and cost functional gradient are derived in Appendix A2 and A3, respectively. Finally, the comparison between a finite difference approximation of the cost function gradient and the adjoint evaluation is performed in Appendix A4.

A1 Continuous adjoint method

We adopt the standard L^2 inner product over the time interval $[0,T]$ and simulation domain Ω

$$(\boldsymbol{a},\boldsymbol{b}) = \int_0^T \iint_\Omega \boldsymbol{a}\cdot\boldsymbol{b}\,\mathrm{d}\boldsymbol{x}\mathrm{d}t \tag{A1}$$

where $\boldsymbol{a}$ and $\boldsymbol{b}$ are two generic vectors. Moreover, we denote with $\boldsymbol{\psi} = \left[u_1, v_1, u_2, v_2, p_1, p_2\right]$ the vector containing the state variables and with $C_T = C_T(x,y,t)$ the control parameter.

The reduced cost functional is defined as

$$\tilde{\mathcal{J}}(C_T) = \int_0^T \iint_\Omega \mathcal{K}\left(\boldsymbol{\psi}(C_T), C_T\right)\,\mathrm{d}\boldsymbol{x}\mathrm{d}t \tag{A2}$$

where

$$\mathcal{K}\left(\boldsymbol{\psi}(C_T), C_T\right) = -\beta\|\boldsymbol{U}_1\|C_p B(x,y)\left(\|\boldsymbol{U}_1\|^2 + 3\boldsymbol{U}_1\cdot\boldsymbol{u}_1\right). \tag{A3}$$

The gradient of the reduced cost functional $\nabla\tilde{\mathcal{J}}$ is interpreted as the Riesz representation of the Gâteaux derivative operator at C_T in any arbitrary direction δC_T

$$\tilde{\mathcal{J}}_{C_T}(\delta C_T) \equiv \frac{\mathrm{d}}{\mathrm{d}\alpha}\tilde{\mathcal{J}}(C_T + \alpha\delta C_T)\bigg|_{\alpha=0} = \left(\nabla\tilde{\mathcal{J}}, \delta C_T\right) \qquad \forall\,\delta C_T \in \mathcal{H} \tag{A4}$$

where $\mathcal{H}$ denotes the control Hilbert space.

Next, we define the state constraints of the optimization problem (i.e., the three-layer model equations) with shorthand notation $\mathcal{N}(\boldsymbol{\psi}, C_T)$. The reduced formulation of the optimization problem implies by definition that $\mathcal{N}(\boldsymbol{\psi}(C_T), C_T) = 0$, therefore we can write the reduced cost functional as

$$\tilde{\mathcal{J}}(C_T) = \mathcal{J}(\boldsymbol{\psi}(C_T), C_T) + \left(\boldsymbol{\psi}^*, \mathcal{N}(\boldsymbol{\psi}(C_T), C_T)\right) \tag{A5}$$

where $\boldsymbol{\psi}^* = [\zeta_1, \chi_1, \zeta_2, \chi_2, \Pi_1, \Pi_2]$ denotes the vector containing the adjoint variables which play the role of Lagrange multipliers. In fact, it is easy to notice that $\tilde{\mathcal{J}}(C_T) = \mathcal{L}(C_T, \boldsymbol{\psi}(C_T), \boldsymbol{\psi}^*)$, where $\mathcal{L}$ is the Lagrangian of the optimization problem in Eq. 16.

Using A4 and A5, the gradient of the reduced cost functional can be expressed as

$$(\nabla\tilde{\mathcal{J}}, \delta C_T) = \left(\frac{\partial\mathcal{K}}{\partial C_T}, \delta C_T\right) + \left(\boldsymbol{\psi}^*, \frac{\partial\mathcal{N}}{\partial C_T}\delta C_T\right) + \left(\frac{\partial\mathcal{K}}{\partial\boldsymbol{\psi}}, \delta\boldsymbol{\psi}\right) + \left(\boldsymbol{\psi}^*, \frac{\partial\mathcal{N}}{\partial\boldsymbol{\psi}}\delta\boldsymbol{\psi}\right) \tag{A6}$$

where $\delta\boldsymbol{\psi} = \mathrm{d}\boldsymbol{\psi}/\mathrm{d}C_T\ \delta C_T$. The adjoint of the operator $\partial\mathcal{N}/\partial\boldsymbol{\psi}$ is given by

$$\left(\boldsymbol{\psi}^*, \frac{\partial\mathcal{N}}{\partial\boldsymbol{\psi}}\delta\boldsymbol{\psi}\right) = \left(\left[\frac{\partial\mathcal{N}}{\partial\boldsymbol{\psi}}\right]^* \boldsymbol{\psi}^*, \delta\boldsymbol{\psi}\right) + BT_1 \tag{A7}$$

where the right-hand side is found using integration by parts. Similarly, the adjoint of $\partial\mathcal{N}/\partial C_T$ is expressed as

$$\left(\boldsymbol{\psi}^*, \frac{\partial\mathcal{N}}{\partial C_T}\delta C_T\right) = \left(\left[\frac{\partial\mathcal{N}}{\partial C_T}\right]^* \boldsymbol{\psi}^*, \delta C_T\right) + BT_2. \tag{A8}$$

The boundary terms BT_1 and BT_2 arise as a result of the integration by parts. Due to spatial- and time-periodicity constraints, it is easy to show that $BT_1 = BT_2 = 0$. Hence, substituting A7 and A8 into A6, we obtain

$$(\nabla\tilde{\mathcal{J}}, \delta C_T) = \left(\frac{\partial\mathcal{K}}{\partial C_T} + \left[\frac{\partial\mathcal{N}}{\partial C_T}\right]^* \boldsymbol{\psi}^*, \delta C_T\right) + \left(\frac{\partial\mathcal{K}}{\partial\boldsymbol{\psi}} + \left[\frac{\partial\mathcal{N}}{\partial\boldsymbol{\psi}}\right]^* \boldsymbol{\psi}^*, \delta\boldsymbol{\psi}\right). \tag{A9}$$

Further, we assume that the adjoint variables satisfy the following relation

$$\left(\frac{\partial\mathcal{K}}{\partial\boldsymbol{\psi}} + \left[\frac{\partial\mathcal{N}}{\partial\boldsymbol{\psi}}\right]^* \boldsymbol{\psi}^*, \delta\boldsymbol{\psi}\right) = 0 \tag{A10}$$

which defines the adjoint equations. Therefore, the adjoint gradient is given by

$$\nabla\tilde{\mathcal{J}} = \frac{\partial\mathcal{K}}{\partial C_T} + \left[\frac{\partial\mathcal{N}}{\partial C_T}\right]^* \boldsymbol{\psi}^*. \tag{A11}$$

A2 Derivation of the adjoint equations

We apply relation A7 for deriving the adjoint of the operator $\partial\mathcal{N}/\partial\boldsymbol{\psi}$. Starting with the velocity perturbations in the wind-farm layer, we have

$$\left(\boldsymbol{\psi}^*, \frac{\partial\mathcal{N}}{\partial\boldsymbol{u}_1}\delta\boldsymbol{u}_1\right) = \int_0^T \iint_\Omega \left[\frac{\partial\delta\boldsymbol{u}_1}{\partial t} + \boldsymbol{U}_1\cdot\nabla\delta\boldsymbol{u}_1 + f_c\boldsymbol{J}\cdot\delta\boldsymbol{u}_1 - \nu_{t,1}\nabla^2\delta\boldsymbol{u}_1 + \frac{\boldsymbol{D}'}{H_1}\cdot\delta\boldsymbol{u}_1 + \frac{\boldsymbol{C}'}{H_1}\cdot\delta\boldsymbol{u}_1 + \right.$$
$$\left. - \frac{1}{H_1}\frac{\partial\boldsymbol{f}^{(1)}}{\partial\boldsymbol{u}_1}\bigg|_{\delta\boldsymbol{u}_1}\right]\cdot\boldsymbol{\zeta}_1\,\mathrm{d}\boldsymbol{x}\mathrm{d}t + \int_0^T\iint_\Omega\left[-\frac{\boldsymbol{D}'}{H_2}\cdot\delta\boldsymbol{u}_1\right]\cdot\boldsymbol{\zeta}_2\,\mathrm{d}\boldsymbol{x}\mathrm{d}t + \int_0^T\iint_\Omega\left[H_1\mathcal{F}^{-1}\Phi(\hat{\Phi})*\nabla\cdot\delta\boldsymbol{u}_1\right]\cdot\Pi_1\,\mathrm{d}\boldsymbol{x}\mathrm{d}t \tag{A12}$$

and by computing an integration by parts we obtain

$$\left(\left[\frac{\partial\mathcal{N}}{\partial\boldsymbol{u}_1}\right]^*\boldsymbol{\psi}^*, \delta\boldsymbol{u}_1\right) = \int_0^T\iint_\Omega\left[-\frac{\partial\boldsymbol{\zeta_1}}{\partial t} - \boldsymbol{U}_1\cdot\nabla\boldsymbol{\zeta}_1 + f_c\boldsymbol{J}\cdot\boldsymbol{\zeta}_1 - \nu_{t,1}\nabla^2\boldsymbol{\zeta}_1 + \frac{\boldsymbol{D}'}{H_1}\cdot\boldsymbol{\zeta}_1 + \frac{\boldsymbol{C}'}{H_1}\cdot\boldsymbol{\zeta}_1 + \right.$$
$$\left. + \frac{\beta}{H_1}\frac{C_T B(x,y)}{\|\mathbf{U}_1\|}\mathbf{U}_1\mathbf{U}_1 + \mathbf{H}\mathbf{U}_1^2\frac{\beta C_T B(x,y)}{H_1}\boldsymbol{U}'\cdot\boldsymbol{\zeta}_1 - \frac{\boldsymbol{D}'}{H_2}\cdot\boldsymbol{\zeta}_2 - H_1\left[\mathcal{F}^{-1}\Phi(\hat{\Phi})(-\boldsymbol{x},-t)*\nabla\Pi_1\right]\right]\cdot\delta\boldsymbol{u}_1\,\mathrm{d}\boldsymbol{x}\mathrm{d}t. \tag{A13}$$

~~Similarly~~ Note that the minus sign in the argument of $\mathcal{F}^{-1}(\hat{\Phi})(-\boldsymbol{x},-t)$ does not come from classical integration by parts. In fact, given three functions $f,g,h\in L^1(\Omega)$, it can be shown that

$$\begin{aligned}\int_\Omega\left[f(x)*g(x)\right]h(x)dx &= \int_\Omega\int_{\Omega'}\left[f(x-x')g(x')dx'\right]h(x)dx\\ &= \int_{\Omega'}\int_\Omega f(-(x'-x))h(x)dx g(x')dx'\\ &= \int_\Omega\left[f(-x)*h(x)\right]g(x)dx.\end{aligned} \tag{A14}$$

where in the second passage we have changed the order of integration (Fubini's theorem). This property allows us to write

$$-H_1\int_0^T\iint_\Omega\left[\mathcal{F}^{-1}(\hat{\Phi})*\delta\boldsymbol{u}_1\right]\cdot\nabla\Pi_1\,\mathrm{d}\boldsymbol{x}\mathrm{d}t = -H_1\int_0^T\iint_\Omega\left[\mathcal{F}^{-1}(\hat{\Phi})(-\boldsymbol{x},-t)*\nabla\Pi_1\right]\cdot\delta\boldsymbol{u}_1\,\mathrm{d}\boldsymbol{x}\mathrm{d}t. \tag{A15}$$

Similarly, for the velocity perturbations in the upper layer, we have that

$$\left(\left[\frac{\partial\mathcal{N}}{\partial\boldsymbol{u}_2}\right]^*\boldsymbol{\psi}^*, \delta\boldsymbol{u}_2\right) = \int_0^T\iint_\Omega\left[-\frac{\boldsymbol{D}'}{H_1}\cdot\boldsymbol{\zeta_1} - \frac{\partial\boldsymbol{\zeta}_2}{\partial t} - \boldsymbol{U}_2\cdot\nabla\boldsymbol{\zeta}_2 + f_c\boldsymbol{J}\cdot\boldsymbol{\zeta}_2 - \nu_{t,2}\nabla^2\boldsymbol{\zeta}_2 + \frac{\boldsymbol{D}'}{H_2}\cdot\boldsymbol{\zeta}_2 + \right.$$
$$\left. - H_2\left[\mathcal{F}^{-1}\Phi(\hat{\Phi})(-\boldsymbol{x},-t)*\nabla\Pi_2\right]\right]\cdot\delta\boldsymbol{u}_2\,\mathrm{d}\boldsymbol{x}\mathrm{d}t. \tag{A16}$$

Following the same procedure for the pressure perturbations p_1 and p_2, we obtain

$$\left(\left[\frac{\partial \mathcal{N}}{\partial p_1}\right]^* \boldsymbol{\psi}^*, \delta p_1\right) = \int_0^T \iint_\Omega \left[-\frac{1}{\rho_0}\nabla\cdot\boldsymbol{\zeta}_1 - \frac{1}{\rho_0}\nabla\cdot\boldsymbol{\zeta}_2 - \frac{1}{\rho_0}\frac{\partial \Pi_1}{\partial t} - \frac{1}{\rho_0}\boldsymbol{U}_1\cdot\nabla\Pi_1\right]\cdot\delta p_1 \,\mathrm{d}\boldsymbol{x}\mathrm{d}t \tag{A17}$$

and

$$\left(\left[\frac{\partial \mathcal{N}}{\partial p_2}\right]^* \boldsymbol{\psi}^*, \delta p_2\right) = \int_0^T \iint_\Omega \left[-\frac{1}{\rho_0}\nabla\cdot\boldsymbol{\zeta}_1 - \frac{1}{\rho_0}\nabla\cdot\boldsymbol{\zeta}_2 - \frac{1}{\rho_0}\frac{\partial \Pi_2}{\partial t} - \frac{1}{\rho_0}\boldsymbol{U}_2\cdot\nabla\Pi_2\right]\cdot\delta p_2 \,\mathrm{d}\boldsymbol{x}\mathrm{d}t. \tag{A18}$$

Using A10, the resulting adjoint equations correspond to

$$\begin{aligned}
&-\frac{\partial \boldsymbol{\zeta}_1}{\partial t} - \boldsymbol{U}_1\cdot\nabla\boldsymbol{\zeta}_1 + f_c\boldsymbol{J}\cdot\boldsymbol{\zeta}_1 - \nu_{t,1}\nabla^2\boldsymbol{\zeta}_1 + \frac{\boldsymbol{D}'}{H_1}\cdot\boldsymbol{\zeta}_1 + \frac{\boldsymbol{C}'}{H_1}\cdot\boldsymbol{\zeta}_1 - \frac{\boldsymbol{D}'}{H_2}\cdot\boldsymbol{\zeta}_2 - H_1\left[\mathcal{F}^{-1}(\Phi\hat{\Phi})(-\boldsymbol{x},-t) * \nabla\Pi_1\right] + \\
&+ \frac{\beta}{H_1}\frac{C_T B(x,y)}{\|\mathbf{U}_1\|}\frac{\beta C_T B(x,y)}{H_1}\boldsymbol{U}_{11+1^2}\cdot\boldsymbol{\zeta}_1 = -\frac{\partial \mathcal{K}}{\partial \boldsymbol{u}_1} && \text{in } \Omega\times(0,T],\\
&-\frac{\partial \boldsymbol{\zeta}_2}{\partial t} - \boldsymbol{U}_2\cdot\nabla\boldsymbol{\zeta}_2 + f_c\boldsymbol{J}\cdot\boldsymbol{\zeta}_2 - \nu_{t,2}\nabla^2\boldsymbol{\zeta}_2 + \frac{\boldsymbol{D}'}{H_2}\cdot\boldsymbol{\zeta}_2 - \frac{\boldsymbol{D}'}{H_1}\cdot\boldsymbol{\zeta}_1 - H_2\left[\mathcal{F}^{-1}(\Phi\hat{\Phi})(-\boldsymbol{x},-t) * \nabla\Pi_2\right] = -\frac{\partial \mathcal{K}}{\partial \boldsymbol{u}_2} && \text{in } \Omega\times(0,T],\\
&-\frac{\partial \Pi_1}{\partial t} - \boldsymbol{U}_1\cdot\nabla\Pi_1 - \nabla\cdot\boldsymbol{\zeta}_1 - \nabla\cdot\boldsymbol{\zeta}_2 = -\rho_0\frac{\partial \mathcal{K}}{\partial p_1} && \text{in } \Omega\times(0,T],\\
&-\frac{\partial \Pi_2}{\partial t} - \boldsymbol{U}_2\cdot\nabla\Pi_2 - \nabla\cdot\boldsymbol{\zeta}_1 - \nabla\cdot\boldsymbol{\zeta}_2 = -\rho_0\frac{\partial \mathcal{K}}{\partial p_2} && \text{in } \Omega\times(0,T].
\end{aligned} \tag{A19}$$

The adjoint momentum equations of the upper layer are homogeneous, since the adjoint wind-farm drag force is felt only indirectly in this layer ($\partial\mathcal{K}/\partial\boldsymbol{u}_2 = 0$). Moreover, also $\partial\mathcal{K}/\partial p_1 = \partial\mathcal{K}/\partial p_2 = 0$. ~~The~~ On the other hand, the adjoint momentum equations of the wind-farm layer are driven by the cost function. Using A3, we obtain

$$\frac{\partial \mathcal{K}}{\partial \boldsymbol{u}_1} = -3\beta C_p B(x,y)\|\boldsymbol{U}_1\|\boldsymbol{U}_1. \tag{A20}$$

Fig. A1 illustrates a planform view of the forward and adjoint solutions in subcritical flow conditions ($F_r = 0.9$). Both solutions are derived assuming a steady-state formulation of the optimization problem. The numerical setup, wind-farm layout and atmospheric state are the ones listed in Table 1. Due to integration by parts, the convective term is negative in the backward equations, causing the flow to propagate upstream (i.e., from right to left of our domain) as displayed in Fig. A1 (bottom row). Moreover, the wind farm acts as a source term and it speeds up the adjoint solution instead of decelerating it, causing an acceleration within the wind-farm area and in the wake region.

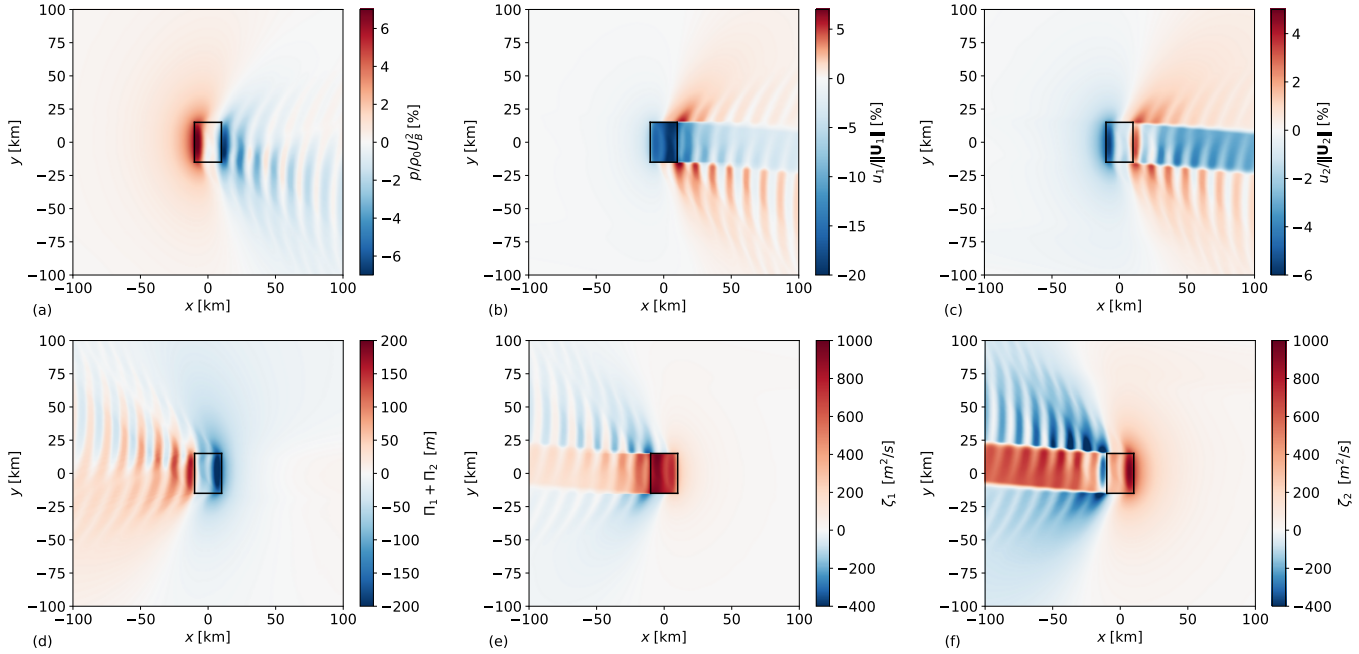

Figure A1. Planform view of (a) pressure perturbation, (b) velocity perturbation in the wind-farm layer, (c) velocity perturbation in the upper layer, (d) adjoint pressure $\Pi = \Pi_1 + \Pi_2$, (e) adjoint velocity field in the wind-farm layer and (f) adjoint velocity field in the upper layer in subcritical ($F_r = 0.9$) flow conditions. The black rectangle indicates the wind-farm region.

A3 Derivation of the gradient

The adjoint gradient of the cost function is derived using relation A11. To compute the adjoint of the operator $\partial\mathcal{N}/\partial C_T$, we need to evaluate the following inner product

$$\left(\boldsymbol{\psi}^*, \frac{\partial \mathcal{N}}{\partial C_T}\delta C_T\right) = \int_0^T \iint_\Omega \left[-\frac{1}{H_1}\frac{\partial \boldsymbol{f}^{(0)}}{\partial C_T}\bigg|_{\delta C_T} - \frac{1}{H_1}\frac{\partial \boldsymbol{f}^{(1)}}{\partial C_T}\bigg|_{\delta C_T}\right]\cdot \boldsymbol{\zeta_1}\,\mathrm{d}\boldsymbol{x}\mathrm{d}t$$
$$= \int_0^T \iint_\Omega \left[\frac{1}{H_1}\beta B(x,y)\frac{\beta B(x,y)}{H_1}\delta C_T \|\boldsymbol{U}_1\|\boldsymbol{U}_1 + \frac{\beta B(x,y)}{H_1}\delta C_T + \frac{1}{H_1}\beta B(x,y)\frac{1}{\|\boldsymbol{U}_1\|}\boldsymbol{U}_{1_1+1_2}\cdot \boldsymbol{u}_1\right]\cdot \boldsymbol{\zeta}_1\,\mathrm{d}\boldsymbol{x}\mathrm{d}t \tag{A21}$$

which is easily rewritten as

$$\left(\left[\frac{\partial \mathcal{N}}{\partial C_T}\right]^* \boldsymbol{\psi}^*, \delta C_T\right) = \int_0^T \iint_\Omega \left[\frac{1}{H_1}\beta B(x,y)\frac{\beta B(x,y)}{H_1}\left(\|\boldsymbol{U}_1\|\boldsymbol{U}_1\cdot\boldsymbol{\zeta}_1 + \frac{1}{\|\boldsymbol{U}_1\|}\boldsymbol{u}_1^\top\cdot\boldsymbol{U}_{1_1+1_2}\cdot\boldsymbol{\zeta_1}\right)\right]\cdot\delta C_T\,\mathrm{d}\boldsymbol{x}\mathrm{d}t. \tag{A22}$$

Moreover, we derive the first term on the right-hand side of A11 using A3, which results in

$$\frac{\partial \mathcal{K}}{\partial C_T} = -\beta B(x,y)\|\boldsymbol{U}_1\|\frac{\mathrm{d}C_p}{\mathrm{d}C_T}\left(\|\boldsymbol{U}_1\|^2 + 3\boldsymbol{U}_1\cdot\boldsymbol{u}_1\right). \tag{A23}$$

Finally, we obtain the gradient expression by substituting A22 and A23 in A11, which gives

$$\nabla\tilde{\mathcal{J}} = \beta B(x,y)\frac{\beta B(x,y)}{H_1}\left[\frac{1}{H_1}\|\boldsymbol{U}_1\|\boldsymbol{U}_1\cdot\boldsymbol{\zeta}_1 - H_1\|\boldsymbol{U}_1\|\frac{\mathrm{d}C_p}{\mathrm{d}C_T}\left(\|\boldsymbol{U}_1\|^2+3\boldsymbol{U}_1\cdot\boldsymbol{u}_1\right)+\frac{1}{H_1\|\boldsymbol{U}_1\|}\boldsymbol{u}_1^{\top}\cdot\boldsymbol{U}_{1_1+1_-^{2'}}\cdot\boldsymbol{\zeta}_1\right]. \tag{A24}$$

A4 Verification of the adjoint gradient

The aim of this paragraph is to asses the quality of the gradient ~~trough~~ through comparison with a finite difference approximation. The comparison is done using a grid resolution of 500 m. All other parameters correspond to the ones listed in Table 1, with $F_r = 0.9$.

We define with

$$\nabla\tilde{\mathcal{J}}_{\mathrm{ADJ}} = \left(\nabla\tilde{\mathcal{J}}, \delta C_T\right) \tag{A25}$$

the directional derivative of $\nabla\tilde{\mathcal{J}}$ along δC_T, where $\nabla\tilde{\mathcal{J}}$ is the gradient computed with A24 and δC_T is a perturbation of the baseline control C_T. Using finite difference, the same directional derivative can be approximated as

$$\nabla\tilde{\mathcal{J}}_{\mathrm{FD}} = \frac{\tilde{\mathcal{J}}\left(C_T+\alpha\delta C_T\right)-\tilde{\mathcal{J}}\left(C_T\right)}{\alpha}+\mathcal{O}(\alpha). \tag{A26}$$

The truncation error of A26 is proportional to the order of magnitude of the step length α. Therefore, α should be as small as possible to limit the discretization error. However, small values of α induce round-off errors due to finite-precision floating-point arithmetic. In other words, relation A26 provides accurate gradient information only for a lower an upper bounded range of step length values.

Next, we define

$$R = \frac{\nabla\tilde{\mathcal{J}}_{\mathrm{ADJ}}}{\nabla\tilde{\mathcal{J}}_{\mathrm{FD}}}, \tag{A27}$$

$$\epsilon = \left|\frac{\nabla\tilde{\mathcal{J}}_{\mathrm{ADJ}}-\nabla\tilde{\mathcal{J}}_{\mathrm{FD}}}{\nabla\tilde{\mathcal{J}}_{\mathrm{FD}}}\right| \tag{A28}$$

where R and ϵ represent the ratio and the relative error between gradient information computed with the adjoint and finite difference method. If the continuous adjoint method provides correct gradient information, we expect $R \simeq 1$ and ϵ to be sufficiently small.

The following generic baseline control is chosen

$$C_T^{\mathrm{B}}(x,y) = C_T^{\mathrm{Betz}}\left[\frac{1}{2}+\frac{1}{5}\cos\left(k_x x+\pi\right)+\frac{1}{5}\sin\left(k_y y+\pi/5\right)\right] \tag{A29}$$

where $C_T^{\mathrm{Betz}} = 8/9$, $k_x = 2\pi/L_x$ and $k_y = 2\pi/L_y$. Ideally, we should validate the adjoint-based gradient against the finite-difference one for all possible perturbations δC_T. However, such validation would require to solve the governing equations (forward and backward) 2.4×10^3 times since the control space has such DOF using this numerical setup. This computation is too expensive, therefore we select a limited class of perturbations given by

$$\delta C_T(x,y) = \cos\left(ak_x x+\pi\right)+\sin\left(bk_y y+\pi/5\right) \tag{A30}$$

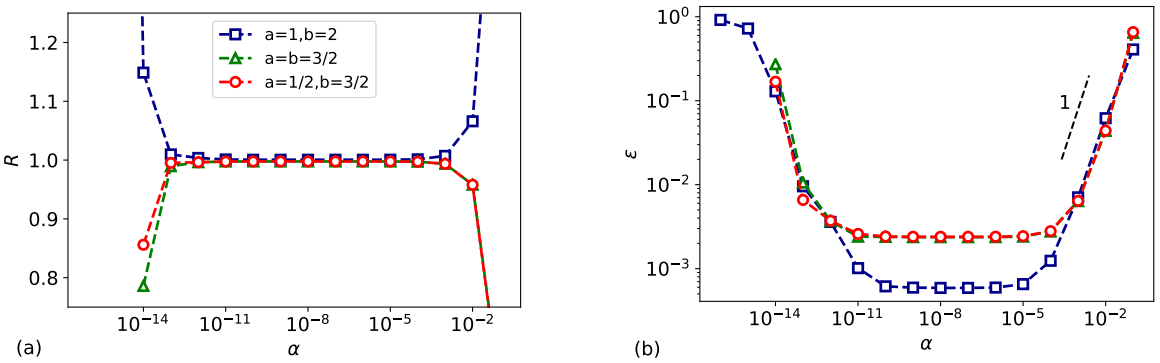

Figure A2. (a) Ratio and (b) relative error between adjoint and finite-difference based gradient.

for different values of a and b.

Results of the comparison are shown in Fig. A2. We can appreciate that for $10^{-11} \leq \alpha \leq 10^{-4}$ the ratio R is very close to unity and the relative error ϵ is in the order of 10^{-4}, showing the typical U-shaped curve (Nita et al., 2016). However, for smaller step length values the relative error increases due to the decreasing arithmetic accuracy of the finite-difference based gradient. The relative error also increases for $\alpha > 10^{-4}$ due to discretization ~~error~~errors. We can appreciate that Fig. A2b displays a first-order truncation error in accordance with relation A26.

Appendix B: Optimal uniform thrust set-point distribution

In the current section, we use the optimization framework derived in Section 2.2 to find an optimal uniform and steady thrust-coefficient distribution that minimizes the gravity-wave induced blockage effects. To avoid confusion, we will denote with C_T^{O} and $C_T^{\mathrm{O,u}}$ the optimal non-uniform and uniform distribution, respectively. The wind-farm layout and the atmospheric state are the ones detailed in Section 3.

Figure B1(a,b) displays the optimal spatially invariant $C_T^{\mathrm{O,u}}$ together with the streamwise profile of C_T^{O} through the center of the farm, and its averaged value over the wind-farm area $\langle C_T^{\mathrm{O}} \rangle$ for the sub- and supercritical case, respectively. Moreover, C_T^{R} denotes the thrust distribution used in the reference model. Interestingly, $C_T^{\mathrm{O,u}}$ corresponds to the average of the non-uniform distribution in both cases. Since C_T^{O} is sensitive to the atmospheric conditions, we expect $C_T^{\mathrm{O,u}}$ to depend as well on the atmospheric state (in fact, we observe a different value of $C_T^{\mathrm{O,u}}$ in sub- and supercritical conditions).

In the current example, the energy gain $\mathcal{G}$ (see Eq. 21) over the reference model configuration obtained with the non-uniform distributions C_T^{O} are 5.3% and 7% for the sub- and supercritical case, respectively. For the optimal uniform distributions, we obtain an energy gain of 5% and 6.6%.

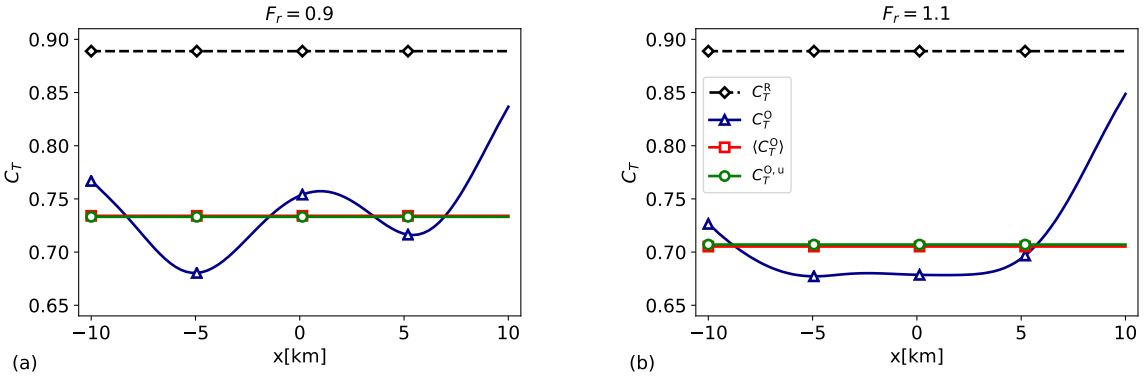

Figure B1. Reference thrust set-point (C_T^{R}), optimal non-uniform thrust set-point (C_T^{O}) and its averaged value over the wind-farm area ($\langle C_T^{\mathrm{O}} \rangle$) and optimal uniform thrust coefficient distribution ($C_T^{\mathrm{O,u}}$) in (a) subcritical and (b) supercritical flow conditions. The C_T^{O} profiles are taken through the center of the farm ($y = 0$).

Appendix C: Grid sensitivity

A grid sensitivity analysis is performed to determine the dependence of the optimization results on the grid cell size. To this end, we fix the size of the numerical domain to $1000H \times 400H$ and we vary the grid resolution spanning from $5H$ to $H/3$, or equivalently from 1.6×10^4 to 3.6×10^6 DOF per layer. The results obtained are compared with the ones derived on a finer grid with resolution equal to $H/4$.

Fig. C1a and Fig. C1b display the cost function and energy gain relative error, respectively, which are computed as

$$\epsilon_{\tilde{\mathcal{J}}} = \left| \frac{\tilde{\mathcal{J}}^{\mathrm{F}} - \tilde{\mathcal{J}}}{\tilde{\mathcal{J}}} \right|, \tag{C1}$$

$$\epsilon_{\mathcal{G}} = \left| \frac{\mathcal{G}^{\mathrm{F}} - \mathcal{G}}{\mathcal{G}} \right| \tag{C2}$$

where $\tilde{\mathcal{J}}^{\mathrm{F}}$ and $\mathcal{G}^{\mathrm{F}}$ are the cost function and energy gain obtained with a $H/4$ grid resolution while $\tilde{\mathcal{J}}$ and $\mathcal{G}$ are the ones obtained with coarser grids. The cost function is evaluated using the reference case setup. The energy gain is obtained using the optimization model described in Section 2. The model setup is reported in Table 1.

Spectral methods are known to have exponential convergence when used for discretizing smooth functions (i.e., $f \in C^\infty$). However, algebraic convergence is attained for functions $f \in C^p$ with $p \geq 0$. Fig. C1 illustrates that we obtain a first-order convergence. This is due to the two-dimensional Heaviside function $B(x, y)$ used for representing the wind-farm footprint, which is discontinuous with discontinuous derivatives. Fig. C1 also confirms that the results of the optimization model are grid-independent. In fact, the cost function and energy gain values change of about 1% and 4% when the number of grid cells is increased by two orders of magnitude (from 10^4 to 10^6). This justifies the use of a coarser grid in the sensitivity study performed in section 4.2.

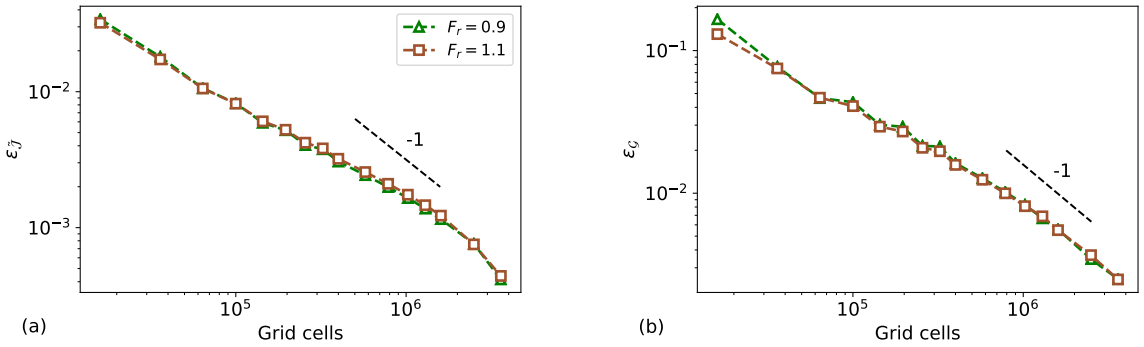

Figure C1. (a) Cost function and (b) energy gain relative error between a grid with resolution $H/4$ and coarser grids in sub- and supercritical flow conditions.

Author contributions. L.L. and J.M. jointly set up the simulation studies in the current work. L.L. performed code implementations and carried out the simulations. L.L. and J.M. jointly wrote the manuscript.

Competing interests. The authors declare that they have no conflict of interest.

Acknowledgements. The authors acknowledge support from the Research Foundation Flanders (FWO, grant no. G0B1518N). The authors thank Prof. Nicole Van Lipzig for useful discussions. The computational resources and services in this work were provided by the VSC (Flemish Supercomputer Center), funded by the Research Foundation Flanders (FWO) and the Flemish Government department EWI.

References

Allaerts, D. and Meyers, J.: Boundary-layer development and gravity waves in conventionally neutral wind farms, J. Fluid Mech., 814, 95–130, 2017.

Allaerts, D. and Meyers, J.: Gravity Waves and Wind-Farm Efficiency in Neutral and Stable Conditions, Boundary-Layer Meteorol., 166, 269–299, 2018.

Allaerts, D. and Meyers, J.: Sensitivity and feedback of wind-farm induced gravity waves, J. Fluid Mech., 862, 990 – 1028, 2019.

Allaerts, D., Vanden Broucke, S., Van Lipzig, N., and Meyers, J.: Annual impact of wind-farm gravity waves on the Belgian-Dutch offshore wind-farm cluster, J. Phys.: Conf. Ser., 1037, 072 006, 2018.

Baker, A. H., Jessup, E. R., and Manteuffel, T.: A technique for accelerating the convergence of restarted GMRES, SIAM J. Matrix Anal. Appl., 26(4), 962–984, 2005.

Barthelmie, R., Pryor, S., Frandsen, S., Hansen, K., Schepers, J., Rados, K., Schlez, W., Neubert, A., Jensen, L., and Neckelmann, S.: Quantifying the impact of wind turbine wakes on power output at offshore wind farms, J. Atmos. Oceanic Technol.,, 27, 1302–1317, 2010.

Bleeg, J., Purcell, M., Ruisi, R., and Traiger, E.: Wind Farm Blockage and the Consequences of Neglecting Its Impact on Energy Production, Energies, 11, 1609, 2018.

Bortolotti, P., Tarrés, H. C., Dykes, K., Merz, K., Sethuraman, L., Verelst, D., and Zahle, F.: IEA Wind Task 37 on Systems Engineering in Wind Energy WP2.1 Reference Wind Turbines, Wind Energy, 2019.

Burton, T., Sharpe, D., Jenkins, N., and Bossanyi, E.: Wind Energy Handbook, Wiley, New York, 2001.

Byrd, R. H., Lu, P., Nocedal, J., and Zhu, C.: A limited memory algorithm for bound constrained optimization, SIAM J. Matrix Anal. Appl., 16, 1190–1208, 1995.

Canuto, C., Hussaini, M. Y., Quarteroni, A., and Zang, T. A.: Spectral Methods in Fluid Dynamics, Springer-Verlag, 1988.

Csanady, G. T.: Equilibrium theory of the planetary boundary layer with an inversion lid, Boundary-Layer Meteorol., 6, 63–79, 1974.

De Los Reyes, J. C.: Numerical PDE-Constrained Optimization, SpringerBriefs in Optimization, 2015.

Fitch, A. C., Olson, J. B., Lundquist, J. K., Dudhia, J., Gupta, A. K., Michalakes, J., and Barstad, I.: Local and mesoscale impacts of wind farms as parameterized in a mesoscale NWP model, Mon. Weather Rev., 140, 3017–3038, 2012.

Frederik, J. A., Weber, R., Cacciola, S., Campagnolo, F., Croce, A., Bottasso, C., and Wingerden, J. W.: Periodic dynamic induction control of wind farms: proving the potential in simulations and wind tunnel experiments, Wind Energy Science, 5, 245–257, 2020.

Gebraad, P., Teeuwisse, F., Wingerden, J., Fleming, P., Ruben, S., Marden, J., and Pao, L.: Wind plant power optimization through yaw control using a parametric model for wake effects - A CFD simulation study, Wind Energy, 19, 95–114, 2016.

Gill, A. E.: Atmosphere-Ocean Dynamics, International Geophysics Series, 30, Academic Press, 1982.

Goit, J. P. and Meyers, J.: Optimal control of energy extraction in wind-farm boundary layers, J. Fluid Mech., 768, 5–50, 2015.

Meyers, J. and Meneveau, C.: Optimal turbine spacing in fully developed wind-farm boundary layers, Wind Energy, 15, 305–317, 2012.

Munters, W. and Meyers, J.: Dynamic Strategies for Yaw and Induction Control of Wind Farms Based on Large-Eddy Simulation and Optimization, Energies, 11, 177, 2018.

Nappo, C. J.: An Introduction to Atmospheric Gravity Waves, International Geophysics Series, 85, Academic Press, 2002.

Niayifar, A. and Porté-Agel, F.: Analytical modeling of wind farms: A new approach for power prediction, Energies, 9, 741, 2016.

Nieuwstadt, F.: On the solution of the stationary, baroclinic Ekman-layer equations with a finite boundary-layer height, Boundary-Layer Meteorol., 26, 377–390, 1983.

Nita, C., Vandewalle, S., and Meyers, J.: On the efficiency of gradient based optimization algorithms for DNS-based optimal control in a turbulent channel flow, Computers and Fluids, 125, 11–24, 2016.

Nocedal, J. and Wright, S. J.: Numerical Optimization, Springer-Verlag,, 1999.

Quick, J., Annoni, J., King, R., Dykes, K., Fleming, P., and Ning, A.: Optimization under uncertainty for wake steering strategies, J. Phys. Conf. Ser., 854, 012036., 2017.

Shamsoddin, S. and Porté-Agel, F.: A model for the effect of pressure gradient on turbulent axisymmetric wakes, J. Fluid Mech., 837, 2018.

Smith, R. B.: Interacting mountain waves and boundary layers, J. Atmos. Sci., 64, 594–607, 2007.

Smith, R. B.: Gravity wave effects on wind farm efficiency, Wind Energy, 13, 449–458, 2010.

Smith, R. B., Jiang, Q., and Doyle, J. D.: A theory of gravity wave absorption by a boundary, J. Atmos. Sci., 63 (2), 774–781, 2006.

Stevens, R. J. A. M.: Dependence of optimal wind turbine spacing on wind farm length, Wind Energy, 19, 651–663, 2016.

Stull, R. B.: An Introduction to Boundary Layer Meteorology, Springer, 1988.

Sutherland, B. R.: Internal gravity waves, Cambridge University Press., 2010.

Volker, P. J. H.: Wake effects of large offshore wind farms - a study of the mesoscale atmosphere, PhD thesis, DTU Wind Energy, 2014.

Wolfe, P.: Convergence conditions for ascent methods, SIAM Rev., 11, 226–235, 1969.

Wu, L. K. and Porté-Agel, F.: Flow Adjustment Inside and Around Large Finite-Size Wind Farms, Energies, 10, 2164, 2017.

Wu, Y.-T. and Porté-Agel, F.: Simulation of turbulent flow inside and above wind farms: model validation and layout effects, Boundary-Layer Meteorol., 146 (2), 181–205, 2013.